

Data and Dynamics Driven Approaches for Forecasting the Red Sea Chlorophyll

Thesis by
Denis Dreano

In Partial Fulfillment of the Requirements
For the Degree of
Doctor of Philosophy

King Abdullah University of Science and Technology, Thuwal,
Kingdom of Saudi Arabia

Insert Date (Month, Year)

The thesis of Your Full Name is approved by the examination committee

Committee Chairperson: Your advisor's name

Committee Member: Second name

Committee Member: Third name

Copyright ©Year

Your Full Name

All Rights Reserved

TABLE OF CONTENTS

1	Introduction and Motivation	1
	Phytoplankton and the Red Sea Ecology: Significance, Large-Scale Features, and Applications	1
	Remotely-Sensed Chlorophyll Data: Relevance and Challenges for the Red Sea	6
	Modeling and Forecasting Chlorophyll: Data and Dynamics Driven Ap- proaches, and Applications	10
	Thesis Objectives	17
2	Research Plan	19
	Chapter 1: Dataset Building and Exploration	21
	Chapter 2: Forecasting Chlorophyll Concentration in Regional Aggregates	23
	Chapter 3: A Global Geostatistical Model for Chlorophyll Forecasting . .	25
	Chapter 4: Local Geostatistical Models for Chlorophyll Forecasting . . .	27
	Chapter 5: Assimilation of Regional 1D Ecological Models and Comparison to Statistical Models	29
	Chapter 6: Combining Statistical and Data Assimilative Predictive Models for Improved Chlorophyll Forecasting	31
3	Summary of Progress	33
	Data Preparation	33
	Red Sea Chlorophyll Data Analysis	35
	Red Sea Regional Clustering	35
	A Global Geostatistical Model	37
	Regional 1D Ecological Models	38
	Data Assimilation into 1D Ecological Models	39
	References	45

Appendix	52
-----------------	-----------

Paper 1: Filtering remotely sensed chlorophyll concentrations in the Red Sea using a space-time covariance model and a Kalman Filter	53
---	-----------

Introduction and Motivation

Phytoplankton and the Red Sea Ecology: Significance, Large-Scale Features, and Applications

The Importance of Phytoplankton

Phytoplankton are unicellular, free-floating, photosynthetic algae that live in the upper layers of bodies of water (ocean, lakes, rivers or ponds). There exists a wide diversity of phytoplankton species. Up to date, about 5000 of them have been identified (*Tett and Barton, 1995*). Phytoplankton are also highly variable in sizes, ranging from 0.2 μm for cyanobacteria to 200 μm for the largest species of diatom (*Pal and Choudhury, 2014*). In the oceans, phytoplankton live in the surface layer where there is enough sunlight for photosynthesis.

Phytoplankton play a fundamental role for the ocean ecology. They are at the basis of the marine food web and trap most of the energy used by pelagic ecosystems (*Pal and Choudhury, 2014*). Zooplankton graze phytoplankton, which are in turn consumed by higher trophic levels. It has been estimated that nearly 98% of the ocean primary productivity comes from phytoplankton (*Pal and Choudhury, 2014*). Phytoplankton are also responsible for maintaining the dissolved oxygen level necessary for other species to survive (*Pal and Choudhury, 2014*). High phytoplankton

concentration however may also impact negatively their environment by creating dead zones. When they die and sink, the bacteria that decompose them can consume all the available oxygen (*Pal and Choudhury, 2014*), and this may cause massive mortality in the fauna. Moreover, because of its short life cycle, phytoplankton respond very well to changes in its environment, making it a key parameter to monitor water quality (*Wu et al., 2014*).

Phytoplankton place at the bottom of the marine food chain makes it an important factor for fisheries. Highly productive fishing zones such as the regions in the Arabian seas, Californian coast, north-west African coast and Chilean coast, are caused by the upwelling of cold nutrient rich water favourable to phytoplankton growth (*Mann and Lazier, 2006*). As such, remotely-sensed chlorophyll data have been routinely used since the last decade to help fisheries predict the timing of phytoplankton blooms (*Robinson, 2010*). The El-Nino phenomenon is known to create less favourable conditions for phytoplankton in the Eastern Pacific, resulting in a dramatic reduction of fish catches of fisheries in the western coast of South America (*Robinson, 2010*). In contrast, in the Red Sea, the MEI (Multivariate ENSO Index) has been found to positively correlate with chlorophyll concentration, which may have a important implications for regional fisheries (*Raitos et al., 2015*).

Phytoplankton also plays the role of a biological CO₂ pump and strongly impact the Earth climate (*Mann and Lazier, 2006*). During photosynthesis, phytoplankton captures carbon and releases oxygen. A part of this organic material stays in the food web, either transmitted to higher trophic level, or degraded by bacteria. Another part sinks to the bottom of the ocean to form sediments. It is estimated that phytoplankton accounts for 48% of Earth carbon fixation (*Pal and Choudhury, 2014*).

Red Sea Large-Scale Phytoplankton Dynamics

Typical tropical seas (TTS), such as the Red Sea, are characterized by a highly stratified structure, where warm nutrient-depleted surface water is separated from the cold nutrient-rich deep water by a steep gradient of temperature zone called pycnocline. The pycnocline acts as barrier that limits the upward nutrients flow (*Mann and Lazier*, 2006). As a result, TTS are oligotrophic exhibiting low chlorophyll concentrations. Until recently, marine biologists believed that tropical and subtropical seas should have low productivity. However, recent investigations have contested this idea, suggesting that different upwelling mechanisms (winter deep mixing, storms, eddies, etc) occur in these regions, and bring new nutrients to the surface water (*Mann and Lazier*, 2006).

Despite being an oligotrophic and challenging environment for marine life, the Red Sea has a surprisingly rich and diverse ecosystem (*Raitos et al.*, 2011), and a very well developed coral reef system (*Racault et al.*). The source of nutrient for sustaining such a developed ecosystem is not well understood yet, but the exchange with the open ocean, the atmospheric depositions and transport through the large number of mesoscale eddies in its basin are believed to be major factors (*Raitos et al.*, 2013; *Zhan et al.*, 2014).

Although the Red Sea environment is still relatively well preserved, it is increasingly stressed by human activities. The continuous urbanization and fishing activity contribute to the fragilization of this unique ecosystem (*Acker et al.*, 2008). An abrupt increase of temperature has further occurred in the last decade, which may further threaten its fragile coral reef system (*Raitos et al.*, 2011).

Because of the lack of in-situ measurements, the large-scale phytoplankton dynamics of the Red Sea remain largely unknown (*Raitos et al.*, 2013; *Triantafyllou*

et al., 2014). In very recent studies, remotely-sensed data and computer simulations have been used to improve our knowledge of the ecology of this region (*Raitos et al.*, 2013; *Racault et al.*; *Triantafyllou et al.*, 2013). The Red Sea is deficient in major nutrients (*Weikert*, 1987), and the only significant input of nutrient-rich water comes from the Gulf of Aden (*Yao and Hoteit*, 2015). This explains the general pattern of chlorophyll concentration increase from north to south (*Raitos et al.*, 2013), with the lowest concentration found in the northern central Red Sea, as can be seen in Figure 1.1. The Red Sea also displays a distinct seasonality, with a peak in concentration during winter. A weak summer peak is also observed over the whole Red Sea around July, except in the northernmost region (*Raitos et al.*, 2013). Despite this regularity, a strong interannual variability was observed, with blooms that can reach mesotrophic concentration levels (*Raitos et al.*, 2013). According to *Triantafyllou et al.* (2014), the variations in the Red Sea ecology are mainly driven by physical circulation. In the rest of this section, we explore some of the mechanisms that have been associated to the major features of chlorophyll concentration in the Red Sea.

The exchange of water with the nutrient-rich Gulf of Aden is a major driving mechanism of the Red Sea productivity (*Triantafyllou et al.*, 2014). It is believed to be the most important source of nutrients. The maximum chlorophyll concentration observed in the southern Red Sea during winter is attributed to wind-driven water intrusion (*Raitos et al.*, 2013; *Yao et al.*, 2014a). In Summer, this exchange of water is believed to be the major source of nutrients for the whole Red Sea. The influence of the water intrusion weakens as the latitude increases, explaining the low concentration in the northern half of the Red Sea (*Raitos et al.*, 2013).

Deep convection also plays an important role in allowing nutrient-rich deep water to mix with water of the euphotic zone. Vertical mixing is the most vigorous in the northern extremity of the Red Sea during winter. This explains its higher chlorophyll

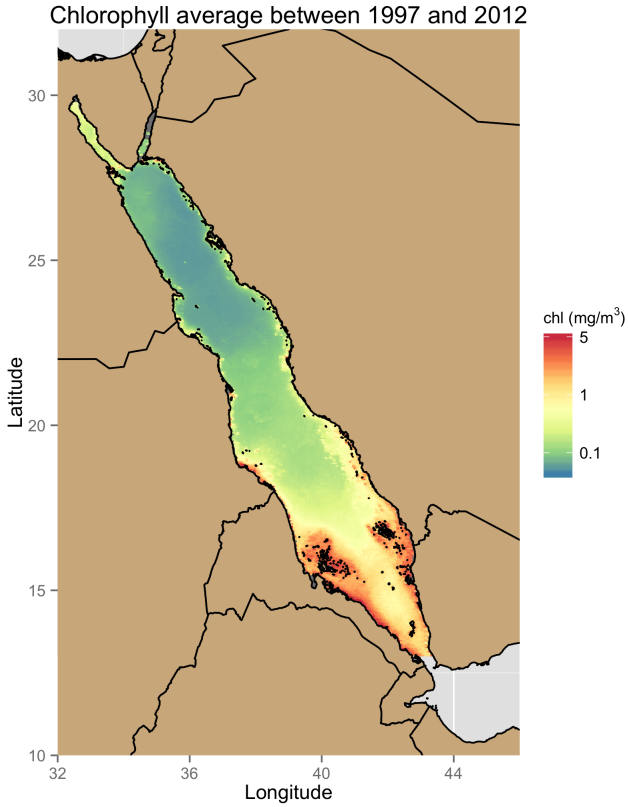


Figure 1.1: Average chlorophyll concentration from CCI data

concentration compared to the north-central Red Sea, a region of weak mixing (*Raittos et al.*, 2013). The northern Red Sea mixing is believed to be mainly driven by wind (*Raittos et al.*, 2013).

The Red Sea circulation is strongly influenced by mesoscale eddies (*Yao et al.*, 2014a,b; *Zhan et al.*, 2014) which may have important impact on its primary productivity (*Zhai and Bower*, 2013). In particular, the anti-cyclonic eddy in the central Red Sea is believed to drive the June concentration peak and the summer productivity of this region, by transporting nutrients and/or phytoplankton from the adjacent coral reefs (*Raittos et al.*, 2013). In the northern Red Sea, a cold-core eddy plays a role in enhancing the vertical mixing in this region (*Raittos et al.*, 2013).

Aerial depositions of dust could also be an important input of nutrients into

the Red Sea, but it has been largely left unexplored (*Triantafyllou et al.*, 2014). *Raittos et al.* (2013) noticed for example that sand storms in the Red Sea most frequently happen in June and July, which coincides with the summer chlorophyll peak. Finally, climate mode indices have been shown to be strongly correlated with air-sea heat exchanges in the Red Sea (*Abualnaja et al.*, 2015), and might therefore influence its biology. This has been also recently confirmed in another study by *Raittos et al.* (2015), who have shown that El Nino has a positive impact on the chlorophyll concentration, by strengthening the wind transporting nutrients into the Red Sea from the Gulf of Aden.

Remotely-Sensed Chlorophyll Data: Relevance and Challenges for the Red Sea

Measuring Chlorophyll Concentration

Chlorophyll is a molecule present in algae, phytoplankton and plants that is critical for photosynthesis. It is a poor absorber of green light, and is responsible for the coloration of plants (*Pal and Choudhury*, 2014). When phytoplankton are present in high concentrations, the water usually takes a detectable green coloration (it may also take a red or blue coloration depending on the type of dominating phytoplankton) (*Robinson*, 2010). This offers an efficient way to measure the phytoplankton concentration from space.

In-situ measurement of chlorophyll concentration can be gathered through scientific cruises, buoy stations or gliders (unmanned submarines). These methods are expensive to deploy and therefore generally have limited temporal and spatial coverage (*Robinson*, 2010). Political issues, as in the Red Sea, as well as security issues,

as in the Arabian Sea, set also barriers to in-situ measurements.

Satellite measurements of chlorophyll provide excellent proxies for phytoplankton concentrations with a good temporal and spatial coverage (*Robinson*, 2010). The SeaWiFS, MODIS and MERIS missions have provided an uninterrupted coverage of global ocean since 1997. High-resolution maps of daily chlorophyll concentration are freely accessible to the scientific community (*McClain*, 2009). Despite some limitations, such as missing data due to cloud coverage and sunglint, or problematic values in coastal areas, remotely-sensed chlorophyll concentrations are intensively used by the scientific community. In regions, like in the Red Sea, where little in-situ measurements are available, these constitute the most important data source (*Raittos et al.*, 2013; *Brewin et al.*, 2013).

Limitation of Remotely-Sensed Chlorophyll Data in the Red Sea

The quality of remotely-sensed chlorophyll data products such as MODIS and SeaWiFS in the Red Sea is comparable to that of the rest of the global ocean for case I waters (open sea) (*Brewin et al.*, 2013). However, the data contains a large amount of missing values because of persistent clouds, sun-glint and sensor saturation (*Racault et al.*). This problem is particularly acute during the summer in the southern Red Sea where the data coverage is almost null (*Racault et al.*), as shown in Figure 1.2.

Chlorophyll concentration estimation in optically complex case II waters is a recurrent problem in this remotely-sensed data that particularly affects the southern Red Sea. In this region, the remotely sensed chlorophyll data could be overestimated (*Raittos et al.*, 2013). However, all high values are not necessarily wrong, as highly productive coral reefs are also present in this region (*Raittos et al.*, 2013). These

values have however not been validated yet, mainly because of the lack of in situ measurements (*Raittos et al.*, 2013).

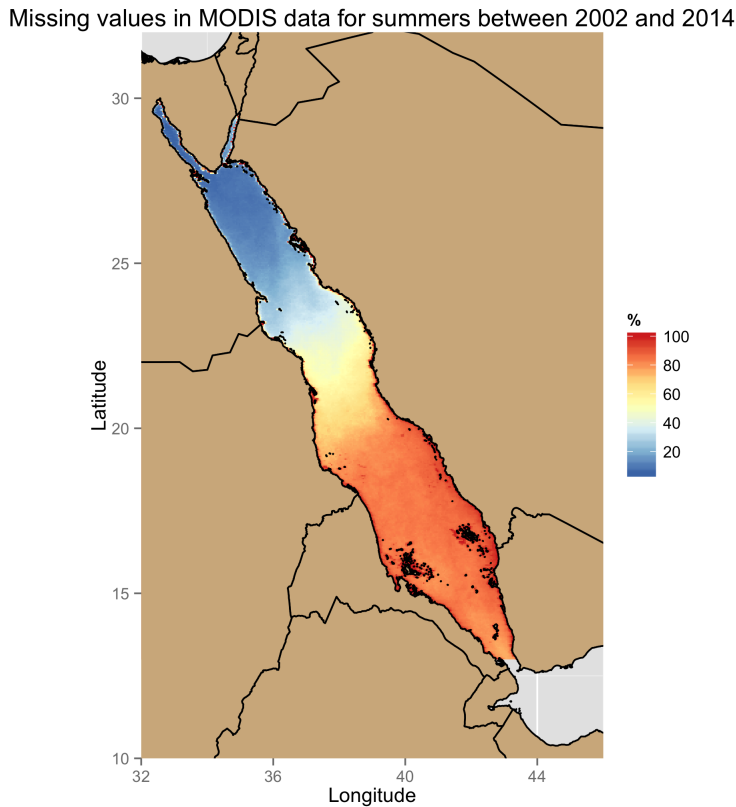


Figure 1.2: Percentage of missing values in the MODIS chlorophyll dataset

One solution to missing and bad values is to apply a data filling algorithm, of which one of the most popular algorithm is the Date INterpolating Empirical Orthogonal Functions (DINEOF), which is an EOF based data filling approach introduced by *Beckers and Rixen* (2003). In *Sirjacobs et al.* (2011), it has been employed to fill chlorophyll data with 70% of missing values. *Taylor et al.* (2013) compared DINEOF with other EOF-based reconstruction algorithms, suggesting that the former is a better method for data filling. DINEOF has been further employed in several other chlorophyll studies (*Miles and He*, 2010; *Waite and Mueter*, 2013), and has also been used for multivariate reconstruction of SST fields using chlorophyll data in *Alvera-*

Azcárate et al. (2007).

The OC-CCI is a new chlorophyll data product that considerably increases the Red Sea coverage. It is a merged product from the SeaWiFS, MODIS and MERIS data missions. Overall, it achieves a 75-80% coverage in the entire Red Sea basin against 50-65% for a single sensor (*Racault et al.*). During the summer, the improvement in coverage is dramatic, as shown in Figure 1.3. This is mostly due to the use of the POLYMER algorithm (*Steinmetz et al., 2011*) that allows to exploit MERIS data collected during hazy conditions. This new dataset has not been fully studied to revisit the assumptions made on the large-scale Red Sea phytoplankton productivity.

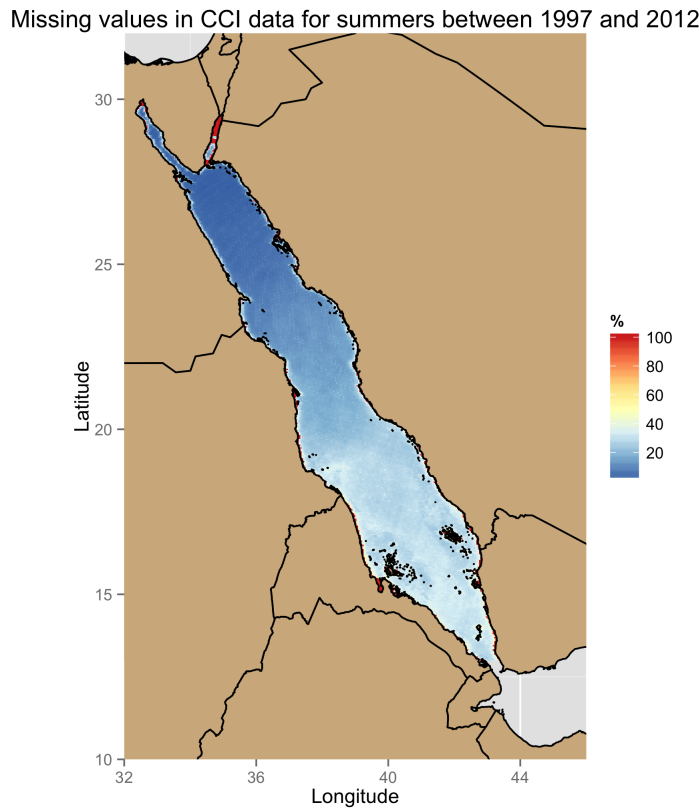


Figure 1.3: Percentage of missing values in the CCI chlorophyll dataset

Modeling and Forecasting Chlorophyll: Data and Dynamics Driven Approaches, and Applications

Why Modeling Chlorophyll?

Computer models are useful to identify causes behind observed chlorophyll patterns.

Many hypotheses have been made about the drivers of chlorophyll concentration in this regions, but some of them have not been investigated through models until very recently. The role played by the exchange of water with the Gulf of Aden and winter overturning in the northern Red Sea have been successfully modeled with a 3D coupled physical-ecological model (*Yao et al.*, 2014a,b; *Triantafyllou et al.*, 2014). However, the interaction between the open sea and coral reefs, and the role of atmospheric depositions have not been investigated yet. Models, can also be helpful for understanding governing dynamics affecting the chlorophyll concentration. In particular, the interaction between the productivity level of the different regions of the Red Sea is yet to be explored.

Model predictions of chlorophyll concentration also have practical applications for fisheries. Furthermore, phytoplankton blooms can be harmful to humans and marine life and are closely monitored in many regions of the world (*Pettersson and Pozdnyakov*, 2013). In the Red Sea, where tourism and aquaculture are developing, it is likely to become a concern too. Phytoplankton is also directly, and indirectly through zooplankton, the cause of microfouling that affects desalination plants. In 2008-2009, a red tide forced the shutdown of desalination plants along the Gulf of Oman and the Arabian Gulf (*Richlen et al.*, 2010).

Deterministic Models

Ecological Models

There is a rich literature on the modeling of marine ecosystems based on a set of mathematical equations governing the ecosystem variability and dynamics (see *Fennel and Neumann* (2004) for an introduction). In these models the interactions of complex physical, chemical and biological processes are modeled by differential equations that represent the flow of carbon, nitrogen, phosphate and silicon. In these models, the biota is usually divided into trophic levels, and can be further divided by feeding methods and size classes (*Baretta et al.*, 1995; *Triantafyllou et al.*, 2014).

Ecological deterministic models vary widely in complexity depending on the number of chemical, biological and ecological processes represented. These can be as simple as the nutrient-phytoplankton-zooplankton (NPZ) model (*Anderson*, 2005) that only uses three variables representing two trophic levels and nitrate, or as complex as the European regional seas ecosystem model (ERSEM) that has dozens of variables (*Baretta et al.*, 1995). NPZ models are extensively used because of their simplicity and capacity to model the large-scale features of marine ecosystems (*Anderson*, 2005). ERSEM has recently been coupled to the MITgcm circulation model to simulate the Red Sea ecology (*Triantafyllou et al.*, 2014). The complexity of these models makes them difficult to parametrize when not enough data are available, which is usually the case in many marginal seas (*Anderson*, 2005). Ecological models can be subject to important sources of uncertainties. These can be due to imperfect modeling assumptions, poorly known initial conditions and physical forcing, and approximative parametrization schemes (*Edwards et al.*, 2015). These set important limitations on the ecosystem models simulation, often causing large deviations of the models outputs from reality.

Data Assimilation

Data assimilation is used to improve the simulations of ecological dynamical models and enhance their forecasting capabilities by constraining their predictions with available observations (*Edwards et al.*, 2015). Such prediction capabilities are now deployed in operational systems, for example to assess the impact of human activities on the ecosystem of the Gulf of Pagasitikos (*Korres et al.*, 2012). The deployment of a similar forecasting system in the Red Sea is currently under development (*Triantafyl-lou et al.*, 2014). Hindcasting, the estimation of unobserved variables, is another application of assimilation systems. *Ciavatta et al.* (2011) showed that data assimilation of ocean color data may improve the seasonal and annual hindcast of non-assimilated biogeochemical properties in the shelf area of Western English Channel. Data assimilation can also be used for reanalysis, to provide estimates of biogeochemical distributions of the past (*Fontana et al.*, 2013).

In the marine ecology modeling community, three assimilation schemes have been widely used: the Ensemble Kalman filters (EnKF), the Singular Evolutive Extended Kalman filter (SEEK), and its ensemble variant, the Singular Evolutive Interpolated Kalman filter (SEIK). The EnKF, a Monte Carlo-based approximation of the Kalman Filter, has been used in *Ciavatta et al.* (2011, 2014). This scheme may however suffer from sampling errors when the ensemble size is smaller than the number of observations, as is usually the case when assimilating remotely-sensed data (*Nerger et al.*, 2005; *Altaf et al.*, 2014). SEEK is a reduced-rank variant of the Extended Kalman filter (EK). It was introduced for efficient data assimilation into large scale ocean models. It is based on the projection of the error covariance onto a low dimensional space. SEEK has a long history in data assimilation for marine ecology models and is still extensively used in recent studies (*Fontana et al.*, 2013; *Korres et al.*, 2012;

Butenschön and Zavatarelli, 2012). SEIK is an ensemble variant of the SEEK and a deterministic version of the EnKF that do not suffer from observations sampling errors, as it updates the filter forecast and its covariance exactly as in the Kalman filter. It therefore requires a resampling step to generate a new analysis ensemble for the next forecast step. SEIK has been used by *Triantafyllou et al.* (2013); *Korres et al.* (2012). *Korres et al.* (2012) shows that SEIK and SEEK are both comparably robust assimilation methods for highly nonlinear systems. *Hoteit et al.* (2005) has suggested however that SEIK outperforms SEEK using a highly nonlinear model.

Predicting the state of ecological models is a challenging problem for state-of-the-art data assimilation schemes (*Edwards et al.*, 2015). First, biogeochemical variables are usually positive concentration, whereas Kalman filters expect Gaussian variables, and log-transformation may fail to avoid this issue (*Ciavatta et al.*, 2011). In an attempt to mitigate this problem, *Fontana et al.* (2013) introduced Gaussian anamorphosis transformations. Second, ecological blooms are intermittent and highly nonlinear, conditions that are challenging for Kalman filter-based assimilation schemes (*Hoteit et al.*, 2005). Third, SEIK, EnKF and SEEK project the error covariance onto some subspace, resulting in an underestimation of the estimation error. *Butenschön and Zavatarelli* (2012) studied different ways to propagate the error covariance in order to alleviate this issue. Finally, the model error statistics are required by Kalman-derived filters, but are difficult to estimate. *Triantafyllou et al.* (2013) proposed to use the H_∞ method with SEIK in order alleviate this requirement.

Particle filters represent a class of data assimilation schemes that, unlike Kalman-based filters, do not require any linearity or Gaussianity assumption (*Edwards et al.*, 2015). As such, they might be more suitable for data assimilation into ecosystem models. They have been studied in the case of 0D and 1D ecological models (*Edwards et al.*, 2015), but are still strongly limited by their demanding computational

requirements. The possibility of applying particle filters to large-slace models is currently an active field of research in the data assimilation community (*Edwards et al.*, 2015).

Data-Driven Approaches

Compared to data assimilative ecological models, data-driven statistical models are relatively simpler to develop. Such models are usually relevant when the phenomenon producing the data is dynamically complex to model, or simply poorly understood (*James et al.*, 2013). Various data-driven models have been proposed to predict chlorophyll concentration, mostly in small regions with complex dynamics (see references below). Some statistical models, such as linear regression, Gaussian additive models, or tree regression have the advantage of being easy to interpret (*James et al.*, 2013), and could be used to understand the dynamics driving the chlorophyll concentration (*Raittos et al.*, 2012).

Statistical Models

Statistical and machine learning models have been recently used for estimation and classification problems related to phytoplankton concentrations. One application is the detection of harmful algal bloom from spatio-temporal satellite dataset, that has been addressed by *Gokaraju et al.* (2011) in the Gulf of Mexico using support vector machines. Another application is the estimation of chlorophyll concentration in case II coastal water using satellite radiance data. This problem has been considered by *Kim et al.* (2014) in the west coast of South Korea, and by *Camps-Valls et al.* (2006) using a global dataset of in situ measurements. The former used the support vector regression algorithm, while the latter used the random forest algorithm.

Machine learning algorithms, in particular Artificial Neural Networks, are also

very popular for forecasting regional chlorophyll concentration in regions with very complex dynamics, where deterministic ecological models usually perform poorly. Neural networks are also commonly used for forecasting chlorophyll concentration in fresh as well as in coastal water systems. In *Jeong et al.* (2006), temporal recurrent recursive neural networks have been used and found superior to traditional time-series models for daily forecasts of chlorophyll concentration. *Wang and Yang* (2013) also used recurrent neural networks for forecasting daily chlorophyll in Lake Taihu, China. *Mulia et al.* (2013) combined Neural Network and genetic algorithm for nowcasting and forecasting of the chlorophyll concentration up to two weeks ahead, in the tidal dominated coast of Singapore. Finally, *Lee et al.* (2003) used neural networks for the forecasting of algal bloom with one or two weeks lags in the coastal waters of Hong-Kong.

Geostatistics

Phenomena such as propagation and diffusion play a key role in the chlorophyll spatial concentration, but are difficult to represent without spatial modeling. There is also a difference in the chlorophyll patterns of different regions of the Red Sea, in particular between the nutrient rich southern Red Sea and the oligotrophic northern Red Sea, and between the open ocean and the coastal waters (*Raittos et al.*, 2013). One should also expect the different regions of the Red Sea to interact.

In contrast with the statistical models discussed above, in geostatistical models, the spatial dimension is modeled explicitly by representing the data as a spatial stochastic process (*Gneiting et al.*, 2007). In classical geostatistics, spatial data is modeled as the realization of a two- (or three-) dimensional Gaussian process (*Gneiting et al.*, 2007). Geostatistics can be easily extended to spatio-temporal datasets (*Gneiting et al.*, 2007). Many ways for constructing space-time covariance functions

for these models have been recently proposed (*Gneiting*, 2002; *Cressie and Huang*, 1999; *Stein*, 2005).

The theory of space-time geostatistics is closely related to that of spatial statistics, since the time dimension is treated as an additional dimension. However, the relationship between these two dimensions is derived from a dynamical process, that must be taken into account in the definition of the covariance function (*Gneiting and Guttorp*, 2010). Some space-time covariance models can actually be derived from a physical formulation, such as the frozen fields (*Gneiting and Guttorp*, 2010), or stochastic differential equations (*Brown et al.*, 2000; *North et al.*, 2011).

Physically-derived space-time covariance functions are not commonly used, and the usual approach is to construct them from spatial and temporal covariance functions (*Gneiting and Guttorp*, 2010). One of the simplest forms of covariance function are the separable covariance functions, that are the products of a spatial covariance function and temporal covariance function. These are computationally efficient, but are not suitable to represent space-time interactions (*Cressie and Huang*, 1999; *Stein*, 2005), making them of limited use for modeling physical systems. The Cressie, Huang spectral characterization theorem of space-time covariance functions has opened the door to wider ways of constructing them. For example, *Gneiting* (2002) presented a simple criterion that allows their construction from a very large class of models.

Space-time geostatistical models have been used in a variety of applications. *Hohn et al.* (1993) used it for forecasting the outbreaks of an invasive specie. These methods have also been used in meteorology to model temperature fields (*Handcock and Wallis*, 1994; *North et al.*, 2011) or wind (*Cressie and Huang*, 1999; *Gneiting*, 2002), and in environmental studies for ground-level ozone concentration. These methods have not been investigated for modeling and forecasting chlorophyll concentration.

Thesis Objectives

The Red Sea physical, chemical and ecological processes are complex and poorly understood. Even though ocean color remote-sensing data has revolutionized our understanding of marine ecology, it only provides information about the phytoplankton at the sea surface. Our knowledge is even more limited in the Red Sea, due to the paucity of in situ data. This makes the modeling and forecasting of chlorophyll variability in the Red Sea a very challenging problem.

The goal of this thesis is to develop novel models for efficient forecasting of chlorophyll concentration in the Red Sea. Various statistical and deterministic models will be developed and tested following data and a dynamical-driven approaches. In particular, we will develop efficient approaches to model the Red Sea chlorophyll, explore the possibility of improving the state-of-the-art data assimilative ecosystem modeling, and introduce the use of geostatistics to the field of marine ecology. The merits of both approaches will be compared for the first time in the same region, and under the same conditions. We will also propose ways to efficiently combine both approaches methods for best forecasting of chlorophyll concentration.

Both deterministic and statistical approaches have been used to predict chlorophyll. However, these approaches have never been compared, nor combined in the same problem. A thorough comparison is very much needed. It would provide modelers with a comprehensive foundation for developing their modeling strategy. Combining them may further improve the forecasting skills.

This thesis will also help improving our understanding of the Red Sea ecology. In particular, it will identify possible drivers for the chlorophyll seasonality and interannual variability. We will also identify and characterize the different Red Sea eco-regions. This work has practical applications for the region. In particular, better

forecasting phytoplankton blooms may be extremely important for the operations of the increasing desalination plants and aquaculture activities along the coast of the Red Sea.

Research Plan

The thesis research plan including a description of the thesis chapters is presented here. To tackle the thesis objectives, I have organized the thesis in six chapters that could be partitioned in two major parts. In the first part, the data is collected and analyzed, and then used to construct statistical models for chlorophyll forecasting. The second part will present data assimilative ecological models, and introduce innovative methods for enhancing the state-of-the-art ensemble assimilation methods. Combining statistical and deterministic models will be further explored.

Chapter 1 presents and analysed the dataset that will be used in the following chapters. In chapter 2, we will divide the Red Sea into eco-regions using data clustering techniques. Then, we will fit statistical models for forecasting chlorophyll in these regions. In chapter 3, we will construct a spatio-temporal geostatistical model for the global Red Sea chlorophyll, and use it for forecasting. In chapter 4, this geostatistical model will be refined by using several regional geostatistical models. In chapter 5, assimilative 1D regional deterministic ecological models will be configured and implemented, and the results will be compared to the developed statistical models. Chapter 6, will develop a method to efficiently combine statistical and deterministic models for improving chlorophyll forecasting in the Red Sea.

In the description of each chapter, I will first explain its importance for reaching the thesis objectives. Then, I will list the open scientific questions that will be

addressed in the chapter. An outline of the methodology will be also presented. The chapter description will conclude with a list of expected outcome.

Chapter 1: Dataset Building and Exploration

A preliminary task to statistical data modeling is the gathering, cleaning and exploration of the data. Given the complexity and the size (40 GB) of the dataset, this is not an simple task. This first data analysis will reveal if enough data has been gathered to make meaningful forecasts, and what accuracy we can expect from the models. This chapter will also provide information that will help in designing statistical models: most significant variables, differences between regions, relevant data transformation, etc. Finally, this chapter will identify patterns in the data that will be useful to qualitatively evaluate predictive models.

Open Questions

- Can we efficiently identify outliers in the chlorophyll values?
- Is there a way to efficiently fill the missing values in the chlorophyll dataset?
- Can the data help understanding the mechanisms behind extreme blooms in the Red Sea?
- Will the data support the hypothesizes about the dynamics behind the chlorophyll seasonal variabilities in the Red Sea?

Methods

1. Identify data sources and gather the data.
2. Clean the data and fill in missing values (DINEOF).
3. Align and format the data to build a cleaned dataset.
4. Explore the dataset.

- Study the correlation between chlorophyll and other variables using, linear regression, GAM, data transformations, etc.
- Apply variable selection techniques such as, lasso, single variable regression, or multistep regression, to reduce the number of variables in the model.
- Study the regional aggregation (ACF), to characterize the regional clusters.
- Explore spatiotemporal correlations (hovmoller plots, PCA, variograms) to understand the spatial features of the chlorophyll data.

Expected Outcomes

- A cleaned dataset that can be used in the following chapters.
- A comprehensive exploration of the available data to study chlorophyll variability in the Red Sea.
- A preliminary variable selection.
- A clear picture of the major spatio-temporal patterns in the chlorophyll data.
- A critical evaluation of the current hypotheses about the chlorophyll dynamics in the Red Sea.

Chapter 2: Forecasting Chlorophyll Concentration in Regional Aggregates

The complexity of marine ecosystems is reflected by the chlorophyll data. It is therefore useful to first simplify it by aggregating it spatially. The space-time dynamics of the chlorophyll data reflects the highly nonlinear dynamics of the underlying physical, chemical and biological phenomena. As shown by the north-south gradient and the seasonal behavior, the resulting space-time process is nonstationary in time and in space. The high-dimensionality in space can be reduced by considering a regional aggregation of the data. This would allow us to focus on the global scale phenomena: such as the interactions between neighboring regions, the time-scale of large events and the difference in the physical variables affecting the chlorophyll concentration in each region. These simple predictive models will also be used as a reference for evaluating the more complex models that will be developed in the following chapters.

Open Questions

- Is the biological aggregation of the Red Sea proposed in (*Raitos et al., 2013*) statistically meaningful?
- Can clustering methods be used to identify marine ecological zones based on chlorophyll data?
- Would simple statistical models allow us to identify the causes of chlorophyll blooms and to forecast chlorophyll concentration?

Methods

1. Define the datasets on which the models will be trained and tested, as well as the cross-validation methodology.
2. Apply unsupervised learning algorithms to the dataset to divide the Red Sea into clusters corresponding to different environmental conditions.
3. Build regional statistical models to forecast chlorophyll concentration.
4. Evaluate the models for the prediction of extreme blooms.

Expected Outcomes

- A division of the Red Sea into environmentally distinct regions that has been quantitatively evaluated.
- A critical evaluation of current hypotheses about the chlorophyll dynamics in the Red Sea.
- A lower bound for the performance of more sophisticated models.
- An assessment of the limitation of aggregate methods for Chlorophyll data.
- An understanding of how the treatment of spatial correlations may improve chlorophyll forecasting.

Chapter 3: A Global Geostatistical Model for Chlorophyll Forecasting

Geostatistical methods can be used to construct dynamical models for forecasting the chlorophyll concentrations. Geostatistics is a robust approach to model spatial data. Recently there has been increasing interest for expanding it to model spatio-temporal data. Through the use of Kriging interpolation, these models provide powerful tools for spatio-temporal prediction. As a particular case of Kriging, by predicting the spatial future field given the observation of the present field, one can derive a linear dynamical model for forecasting the data. This linear model may be employed in a filtering setting like the Kalman filter. This is a desirable framework, and is similar to the way deterministic models are employed to compute forecasts given past observations.

Open Questions

- Can we construct a global geostatistical model that fits well enough chlorophyll data in the Red Sea?
- How non-stationary the chlorophyll data is in time and space?
- Which spatio-temporal covariance functions best fit the chlorophyll concentration?
- Can geostatistical methods be employed in a filtering setup?

Method

Most of the work proposed in this chapter has already been accomplished and has been the subject of a paper that is currently under minor revision in Spatial Statistics.

Expected Outcomes

- A new methodology to employ a geostatistical model in a filtering setup.
- A characterization of the space-time non stationarity of the data.
- A framework for using spatial aggregation and geostatistical models in the same model.

Chapter 4: Local Geostatistical Models for Chlorophyll Forecasting

This chapter will bring together the results of the two preceding chapters to develop a geostatistical model that takes into account the large-scale dynamics and the regional spatio-temporal dynamics. In chapter 2, a predictive model is built, to represent the large scales behaviour of the Red Sea, but the spatial dimension inside each region is not considered. We expect local features to play an important role, such as the proximity to the coast, the bathymetry, proximity to other regions or major cities, etc. In task 3, we proposed a methodology to use a geostatistical model in a dynamical fashion to do pixel-scale forecast. In this task, each regions will be modeled separately by a local geostatistical model that can provide local prediction. These models will have access to aggregate covariates from neighboring regions to represent the global scale behaviours.

Open Questions

- What are the most adapted space-time covariance models for chlorophyll data?
- How to use global covariates in a geostatistical model?
- What are the differences in the spatio-temporal correlation of chlorophyll in each region?
- Can the regional behaviour of phytoplankton be accurately predicted?
- What are the spatial features that are important for regional chlorophyll dynamics in the Red Sea?

Methods

- Extract local datasets from previous tasks based on which we will train regional geostatistical models.
- Design the training and test datasets, and the cross-validation method, as in chapter 2.
- Estimate the chlorophyll mean functions for each region as function of the past covariates, to improve the model forecasting skills.
- Fit local geostatistical models to the residuals, to model them as space-time Gaussian processes.
- Evaluate the model predictions and compare the results with chapters 2 and 3.

Expected Outcomes

- A methodology to aggregate local geostatistical models.
- Improved prediction skills compared to the models developed in Chapters 2 and 3.
- An understanding of the differences between the regions that have been identified in Chapter 2.
- A critical evaluation of the space-time covariance models for fitting chlorophyll data.
- A better characterization of the regional chlorophyll dynamics.

Chapter 5: Assimilation of Regional 1D Ecological Models and Comparison to Statistical Models

The three previous chapters focus on constructing increasingly sophisticated statistical models for predicting the chlorophyll concentration in the Red Sea. In this chapter these models will be evaluated against 1D ecological models (ERSEM). The goal of this part will be to identify the merits of each modeling approach, and propose ways in which they can complement each other. 1D ecological models will be run in each of the regions that have been identified in Chapter 2. Available data will also be assimilated into the models using ensemble Kalman-based filtering and smoothing techniques which we will further equip with an efficient expectation-maximization algorithm for parameters estimation.

Open Questions

- Are statistical methods competitive for forecasting chlorophyll concentrations?
- How may statistical and deterministic models complement each other?
- May statistical methods forecast relevant dynamical features?
- Are there significant regional differences in the relative performances of both approaches?
- How best to estimate the parameters of ecological models?

Methods

1. Implement 1D ERSEM models in each of the identified regions.

2. Select and further develop an assimilation scheme and the data that will be assimilated into each regional model.
3. Implement the assimilation scheme.
4. Run the simulation and aggregate the results to allow for comparison with the statistical models introduced in the previous chapters.
5. Define the metrics for comparison between statistical and deterministic models.
6. Conduct the comparison with the statistical models and summarize the results.

Expected Outcomes

- A complete set of measures of the prediction skills of each approach.
- A method to estimate parameters of an assimilative ecological model.
- An understanding of the limitations of geostatistical models to predict nonlinear dynamics.
- Propositions on how the statistical and dynamical approaches may complement each other.

Chapter 6: Combining Statistical and Data Assimilative Predictive Models for Improved Chlorophyll Forecasting

In the previous chapters, we proposed to evaluate the forecasts of the ecological ERSEM model against those of the statistical models we develop in chapters 2 to 4. In this chapter we will study how these two approaches can be complementary. Specifically, we will study the use of statistical forecasts model to improve the forecasts of the ERSEM ecological model. The forecasts of the statistical models will be treated as observations, that can be assimilated by filtering or smoothing schemes implemented with the ERSEM model. This will hopefully lead to improved forecasts. Real observations will be assimilated sequentially when they become available. This method will allow the different ERSEM models implemented on each cluster to indirectly communicate their estimates between each other.

Open Questions

- Can statistical predictive models be used to communicate information between deterministic models?
- Would the access to information about other regions improve the model forecasts?
- What are the global patterns of ecological dynamics in the Red Sea?

Methods

1. Develop a new assimilation scheme to assimilate statistical predictions and improve the 1D regional deterministic models.

2. Define metrics to measure model improvement compared the results of Chapter 5.
3. Prepare training and test datasets, as in previous chapters.
4. Train statistical models to predict chlorophyll as in Chapter 2.
5. Run simulations with assimilation of statistical and real observations.
6. Compare with the results of Chapter 5.

Expected Outcomes

- An improvement in the prediction skills of the dynamically-driven approach.
- A methodology to couple assimilative dynamically-driven regional ecological models through statistical models.
- Insights on the global ecological dynamics of the Red Sea.
- An efficient general approach to model and forecast chlorophyll concentrations.

Summary of Progress

Data Preparation

All the datasets necessary for the analysis has been gathered. Most of it has been downloaded from public sources on the Internet, using Shell and R scripts. The wind dataset has been provided by Yesubabu Viswanadhapalli, and is the result of the assimilation of all available atmospheric satellite and in situ data in the Red Sea into the Weather Research and Forecasting (WRF) regional Red Sea model. There are additional datasets that will be useful for the analysis. These are mainly climate mode time-series such as the Indian Monsoon Index (IMI) and the East Atlantic - West Russian (EAWR) patterns, that are easy to obtain. The downloaded data is listed and described in table 3.1.

So far, the MODIS and CCI data have been cropped over the region of interest, cleaned and exported to the format TIFF, which can be easily read by most software, R in particular. Each dataset has then been aggregated in a single file in the native R raster format. Applying this processing to the remaining grid data should be straightforward. Then, the data will need to be aligned and aggregated on the same temporal and spatial resolution, before aggregating it in table format.

Variable	Description	Mission/Source	Unit	Temporal Resolution	Period	Spatial Resolution
CHL	Chlorophyll	CCI	mg/m ³	8-days	1997-2012	4km
SST	Sea Surface Temperature	MODIS	Celsius	8-days	2002-2015	4km
AOD	Aerosol Optical Depth	MODIS	N/A	daily	2000-2015	28km
CDOM	Colored Dissolved Organic Matter	MODIS	N/A	8-days	2002-2015	4km
NAO	North Atlantic Oscillation Index	NOAA	N/A	daily	1979-2015	N/A
PAR	Photosynthetically Available Radiations	MODIS	Einstein/m ² .Day	8-days	2002-2015	4km
POC	Particulate Organic Carbon	MODIS	mg/m ³	8-days	2002-2015	4km
RAIN	Precipitations	TRMM	mm/h	daily	1998-2015	28km
SOI	Southern Oscillation Index	Australian Bureau of Meteorology	N/A	daily	1999-2015	N/A
SLA	Sea Level Anomaly	Aviso	cm	daily	1993-2013	28km
WIND	Vector Wind Field	Simulated	m/s	3-hourly	2000-2014	10km

Table 3.1: Downloaded data

Red Sea Chlorophyll Data Analysis

The MODIS and CCI chlorophyll data products have been explored and compared. The MODIS data include an important amount of missing data, which may reach 100% during summer in the southern Red Sea, increasing the complexity of any analysis in this region. The CCI data product solves this issue by merging three sources of remotely-sensed chlorophyll data (MODIS, MERIS and SeaWiFS) and using a new algorithm for retrieving chlorophyll values when the cloud cover is important. This increases the coverage to 70% during summer months in the southern Red Sea.

The SeaWiFS chlorophyll data has been used in the submitted companion article of Chapter 3 (see Appendix B). The seasonal signal in the data is strong and has been shown to account for 50% of the variability. The seasonal anomalies display a strong spatio-temporal correlation: the temporal correlation of anomalies is 40%, whereas two locations at 0.5 degrees apart are nearly 60% correlated. Not shown in this article, I also compared the SST and chlorophyll data, and found an important negative correlation. However, when looking at the anomalies, the correlation was not significant, suggesting that the causes of seasonal and interannual variability are distinct.

Red Sea Regional Clustering

I used clustering algorithms in order to derive the Red Sea eco-regions. These were applied to monthly log-concentration of chlorophyll. I used SeaWiFS data, that has been filled using DINEOF. I used the popular K-means, and the Gaussian Mixture Model (GMM) clustering algorithms.

I found that GMM provides more robust results. With any number of clusters,

we obtain a division of the Red Sea into regions of comparable sizes. With 5 clusters, the regions (shown in figure 3.1) are very similar to those identified by *Raittos et al.* (2013). Contrary to the purely latitudinal division proposed by the former, we observe that the separation between clusters is curved at the position of major Red Sea eddies. The fact that the curvature is oriented toward the south suggests that most nutrients propagate northward from the Gulf of Aden.

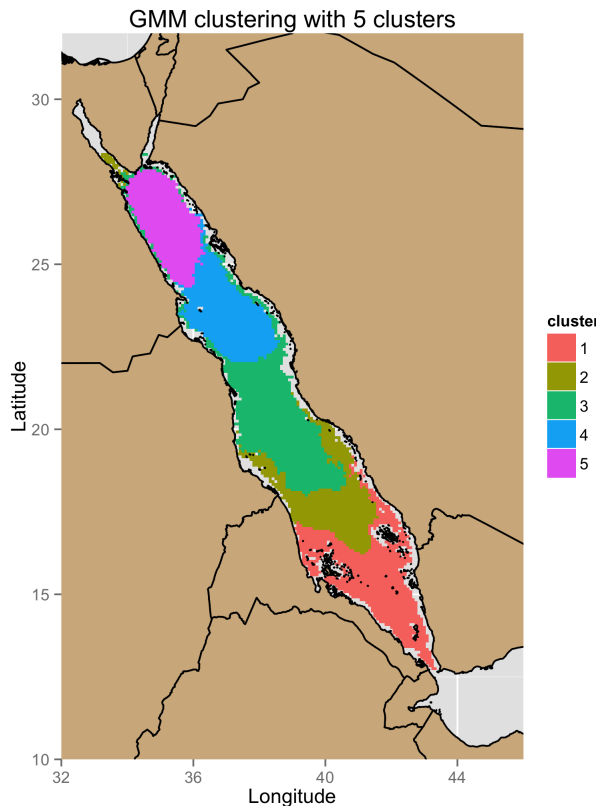


Figure 3.1: Clustering of Red Sea using GMM, with filled monthly SeaWiFS chlorophyll data.

In Chapter 2, I plan to use the dataset constructed in Chapter 1. By using CCI chlorophyll data instead of SeaWiFS, the need for data filling is minimized. This is desirable, as data filling may introduce biases. It will also be possible to use additional variables. For example, we can expect the temperature and the bathymetry to have a large impact on the Red Sea phytoplankton biology. Sea level anomaly can be useful

in that it indicates the presence of mesoscale eddies. Finally, alternative clustering algorithms will be tested.

A Global Geostatistical Model

The research described in Chapter 3 of the thesis has mostly been done and, is the object of an article currently under review. The current version of the manuscript can be found in the appendix. We include the abstract below:

A statistical model is proposed to filter satellite-derived chlorophyll concentration from the Red Sea, and to predict future chlorophyll concentrations. The seasonal trend is first estimated after filling missing chlorophyll data using an Empirical Orthogonal Function (EOF)-based algorithm (Data Interpolation EOF). The anomalies are then modeled as a stationary Gaussian process. A method proposed by Gneiting (2002) is used to construct positive-definite space-time covariance models for this process. After choosing an appropriate statistical model and identifying its parameters, Kriging is applied in the space-time domain to make a one step-ahead prediction of the anomalies. The latter serves as the prediction model of a reduced-order Kalman filter, which is applied to assimilate and predict future observations of chlorophyll concentrations. The proposed method decreases the root mean square (RMS) prediction error by about 11% compared with the seasonal prediction.

Regional 1D Ecological Models

The 1D regional ecological models have been configured and are operational. Three models will be used: for the northern, central and southern Red Sea. The extreme south of the Red Sea is not modeled, as its dynamics is poorly understand and no in situ data are available to validate the satellite products. The ecology is modeled with ERSEM, and the hydrodynamics is modeled with the MITgcm.

The physical forcing from the MITgcm are those of *Yao et al.* (2014a,b), in which a simulation of the Red Sea and part of the Gulf of Aden circulation was run over 50 years. The NCEP data were used for atmospheric forcing, and the data from the group Estimating the Circulation and the Climate of the Ocean (ECCO) for the open boundary conditions in the Gulf of Aden. The output of the 50 years run are used for the temperature and vertical circulation at the modeled points.

ERSEM simulates the complete water column with the pelagic and benthic ecosystems, as well as their coupling. The equations model the flow of carbon, nitrogen, phosphorus and silicon in the ecosystem. Living organisms are modeled in terms of population processes (growth and mortality) and physiological processes (ingestion, respiration, excretion, and egestion). The biota is divided into functional groups according to their trophic levels: producers (phytoplankton), consumers (zooplankton) and decomposers (bacteria), and further subdivided according to their sizes (*Baretta et al.*, 1995).

The ecological models are initialized from the results of a 3D ecological simulation of the Red Sea (*Triantafyllou et al.*, 2014). The nutrient concentrations are initialized using values from the World Ocean Atlas 2005 (WOA 2005). We show the model outputs for the northern Red Sea (Figure 3.2), the central Red Sea (Figure 3.3), and the southern Red Sea (Figure 3.4). The models are able to reproduce the

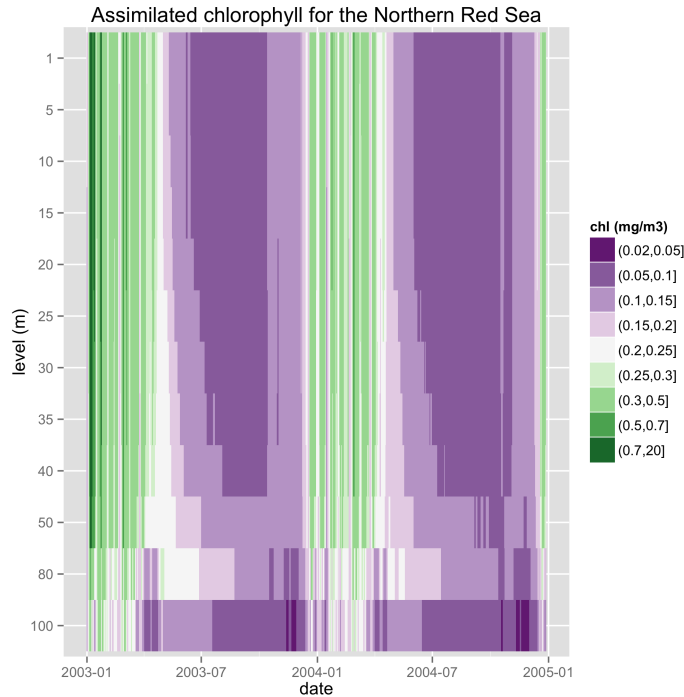


Figure 3.2: Assimilated chlorophyll in the northern Red Sea

seasonality of chlorophyll concentration, with high values in winter and lower values in the summer. As noticed in *Raittoss et al.* (2013), the winter blooms are associated with deep mixing, particularly in the northern Red Sea. During summer, there is a subsurface chlorophyll maximum in the three regions.

Data Assimilation into 1D Ecological Models

Two assimilation schemes for the ecological models have been implemented and are operational: SEIK and hybrid-SEIK, with the hybrid approach implemented as described in *Hamill and Snyder* (2000). The scheme is called hybrid as it combines the flow-dependent background estimates from the ensemble of an EnKF with a static background, taken for example from a three-dimensional variational 3DVAR system. The idea behind it is to complete the rank-deficient EnKF background by

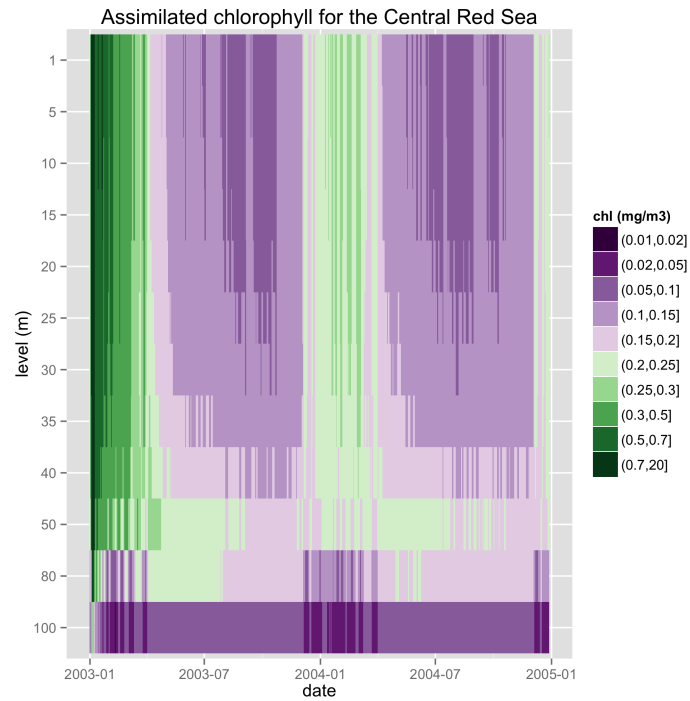


Figure 3.3: Assimilated chlorophyll in the central Red Sea

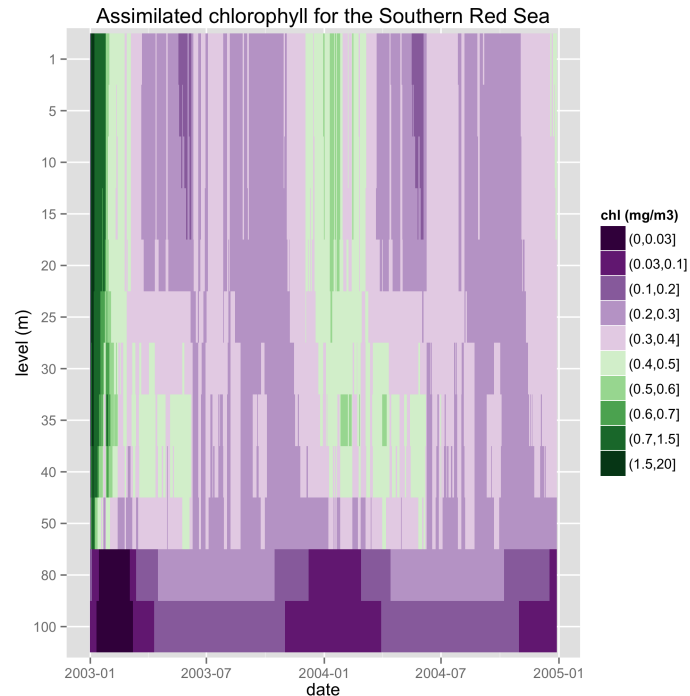


Figure 3.4: Assimilated chlorophyll in the southern Red Sea

another background that has been designed to capture the climatological variability of the system. In our hybrid implementation, the covariance is a linear combination of the 3DVAR covariance and the time-evolving SEIK covariance matrix. We plan to investigate other assimilations scheme, in particular the EnKF.

The problem of optimal filtering can be solved exactly by the Kalman Filter for linear systems. For nonlinear models, one can use the Extended Kalman (EK) filter, in which the model is linearized by computing the error covariance function. However, when the state is large, as is often the case for oceanographic applications, the EK is intractable. In that case, SEEK can be used, where the error covariance function is projected into a smaller subspace. This subspace evolves to ensure that most of the error is represented and filtered out. SEIK can be viewed as an ensemble variant of the SEEK, where the error covariance function is represented exactly by an ensemble of states. This avoids the computation of model gradients, and allows the assimilation scheme to perform better when this model is strongly non-linear. SEIK has been shown to be efficient for large-scale 3D ecosystem data assimilation (*Triantafyllou et al.*, 2003).

We show the chlorophyll surface concentration predicted by the models (with and without assimilation), and the satellite measurements in the three regions in Figures 3.5, 3.6 and 3.7. The models reproduce the seasonality of the chlorophyll concentration with low concentrations in the summer, and a winter bloom. However, the model tends to overestimate the chlorophyll concentration in winter in the northern Red Sea, and to underestimate it in the summer in the southern and central Red Sea. Furthermore, the summer bloom in the southern Red Sea is not well predicted. However, the assimilation is able to correct these biases, and leads to better estimates of chlorophyll concentration.

The Expectation-Maximization (EM) scheme to estimate the filter parameters has

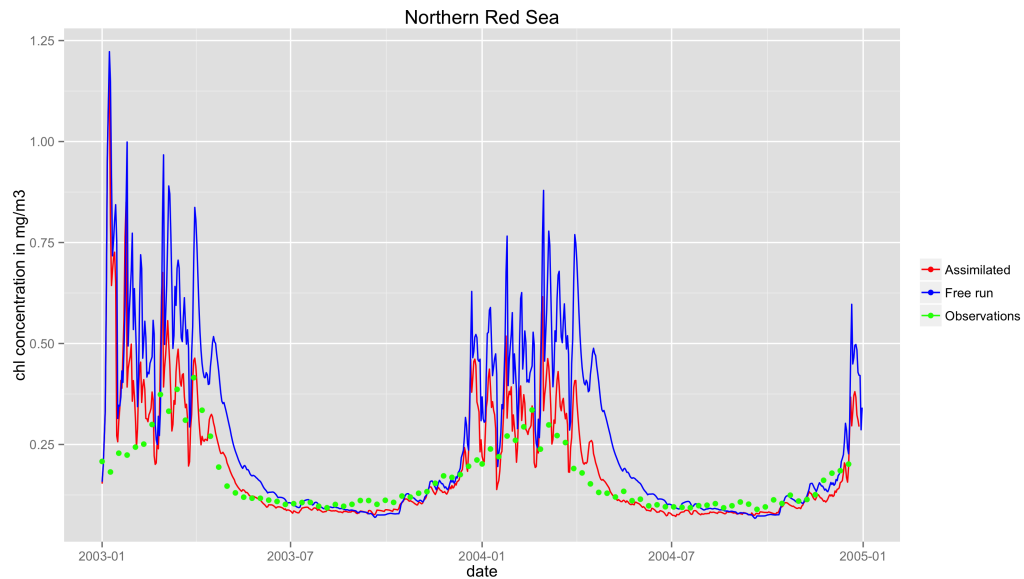


Figure 3.5: Surface chlorophyll in the northern Red Sea from CCI data, assimilated, and non assimilated 1D ecological model

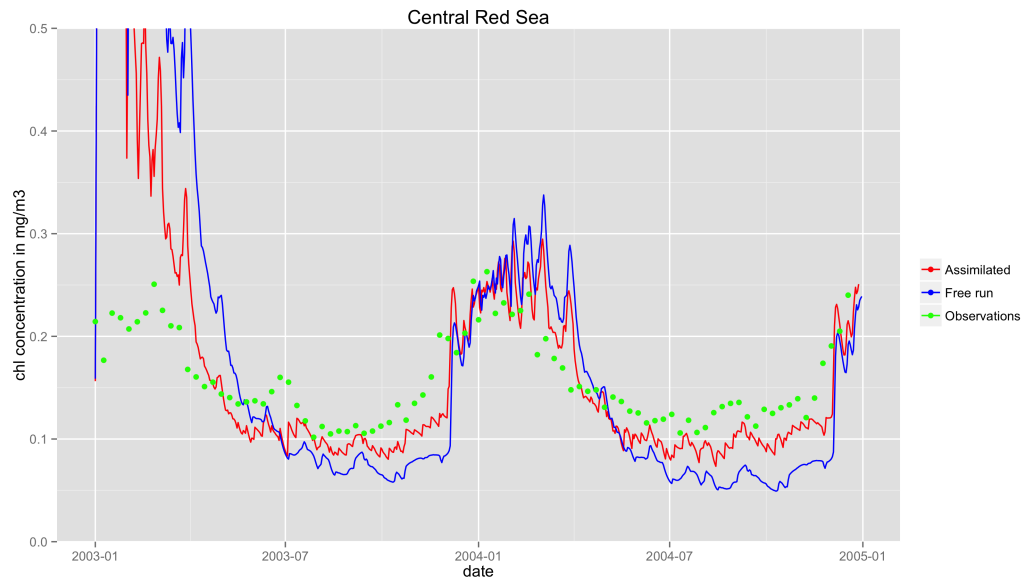


Figure 3.6: Surface chlorophyll in the central Red Sea from CCI data, assimilated, and non assimilated 1D ecological model

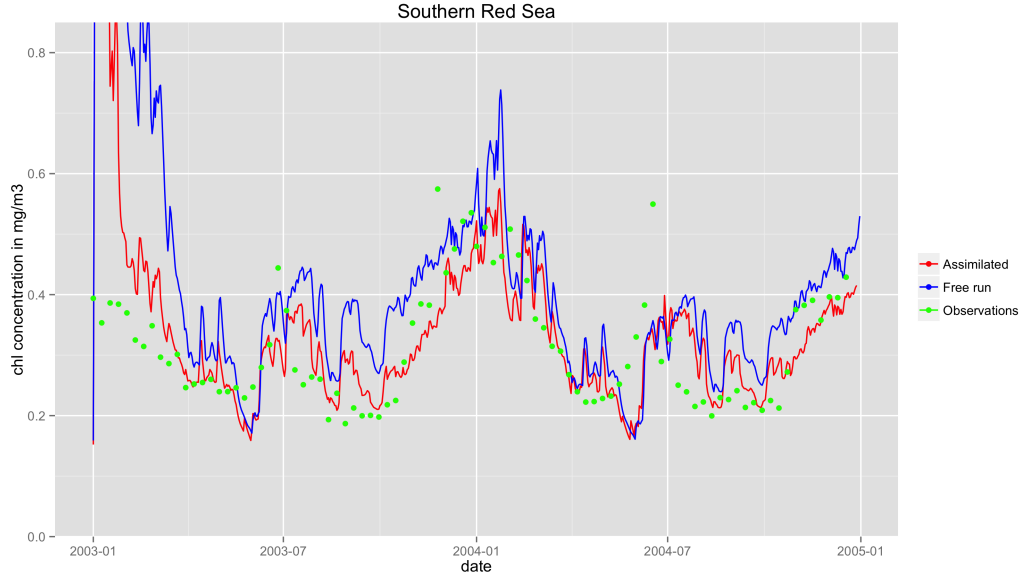


Figure 3.7: Surface chlorophyll in the southern Red Sea from CCI data, assimilated, and non assimilated 1D ecological model

also been derived. It is similar to that proposed by *Tandeo et al.* (2014), which we generalize to nonlinear models. The scheme will be further extended to estimate of the observation and model covariance errors. We outline the steps of the EM scheme hereafter.

We consider the state-space system:

$$\mathbf{x}_k = f_k(\mathbf{x}_{k-1}) + \boldsymbol{\eta}_k, \quad k = 0, \dots, K \quad (3.1)$$

$$\mathbf{y}_k = h_k(\mathbf{x}_k) + \boldsymbol{\varepsilon}_k, \quad k = 1, \dots, K. \quad (3.2)$$

The first equation is the state equation, where \mathbf{x}_k is a vector representing the state of the system (unknown), f_k is the nonlinear model that integrates the state between time t_{k-1} and t_k , and $\boldsymbol{\eta}_k \sim N(0, Q)$ iid is the model error. The second equation is the measurement equation, where \mathbf{y}_k is the observation available at time t_k , h is the observation operator that maps the system state to the observation, and $\boldsymbol{\varepsilon}_k \sim N(0, R)$ iid is the measurement error. The initial state follows a distribution $\mathbf{x}_0 \sim N(\mathbf{x}_b, B)$.

We use the EM scheme in order to estimate the unknown parameters Q , R , \mathbf{x}_b , and B that we regroup under the variable Θ . EM is an iterative procedure to compute the maximum likelihood estimator:

$$\Theta_{\text{ML}} = \arg \max(\log p(\mathbf{y}_{1:K} | \Theta)), \quad (3.3)$$

when it is impossible to analytically express the function to optimize. $\mathbf{y}_{1:K}$ designates all the observations from time step 1 to time step K .

Given an initial estimate $\Theta^{(0)}$, the following two steps are iterated until convergence:

Expectation Step: The function $G(\Theta) = E_{|\Theta=\Theta^{(r)}}[\log p(\mathbf{x}_{0:K} | \Theta, \mathbf{y}_{1:K})]$ is computed. In the case where f and h are linear, the distribution can be exactly computed using the Kalman smoother procedure (*Shumway and Stoffer*, 1982). Otherwise, the distribution can be estimated using, for example, an ensemble smoother (*Tandee et al.*, 2014). This is the strategy we use, since the ecological models are nonlinear.

Maximization Step: The function G is maximized to compute a new estimate of the parameters:

$$\Theta^{(r+1)} = \arg \max_{\Theta} G(\Theta). \quad (3.4)$$

EM is guaranteed to converge when G can be exactly computed. Results from preliminary experiments with a linear system showed that EM may still converge when using an ensemble smoother.

REFERENCES

- Abualnaja, Y., V. P. Papadopoulos, S. A. Josey, I. Hoteit, H. Kontoyiannis, and D. E. Raitsos (2015), Impacts of climate modes on air-sea heat exchange in the Red Sea, *Journal of Climate*, doi:10.1175/JCLI-D-14-00379.1, in press.
- Acker, J., G. Leptoukh, S. Shen, T. Zhu, and S. Kempler (2008), Remotely-sensed chlorophyll a observations of the northern Red Sea indicate seasonal variability and influence of coastal reefs, *Journal of Marine Systems*, 69, 191–204, doi:10.1016/j.jmarsys.2005.12.006.
- Altaf, M. U., T. Butler, T. Mayo, X. Luo, C. Dawson, A. W. Heemink, and I. Hoteit (2014), A comparison of ensemble Kalman filters for storm surge assimilation, *Monthly Weather Review*, 142, 2899–2914, doi:10.1175/Mwr-D-13-00266.1.
- Alvera-Azcárate, A., A. Barth, J.-M. Beckers, and R. H. Weisberg (2007), Multivariate reconstruction of missing data in sea surface temperature, chlorophyll, and wind satellite fields, *Journal of Geophysical Research*, 112, C03008, doi: 10.1029/2006JC003660.
- Anderson, T. R. (2005), Plankton functional type modelling: running before we can walk?, *Journal of Plankton Research*, 27(11), 1073–1081, doi:10.1093/plankt/fbi076.
- Baretta, J. W., W. Ebenhöh, and P. Ruardij (1995), The European regional seas ecosystem model, a complex marine ecosystem model, *Netherlands Journal of Sea Research*, 33(3/4), 233–246, doi:10.1016/0077-7579(95)90047-0.
- Beckers, J. M., and M. Rixen (2003), EOF calculations and data filling from incomplete oceanographic datasets, *Journal of Atmospheric and Oceanic Technology*, 20(12), 1839–1856, doi:10.1175/1520-0426(2003)020<1839:Ecadff>2.0.Co;2.

- Brewin, R. J. W., D. E. Raitsos, Y. Pradhan, and I. Hoteit (2013), Comparison of chlorophyll in the Red Sea derived from MODIS-Aqua and in vivo fluorescence, *Remote Sensing of Environment*, 136, 218–224, doi:10.1016/j.rse.2013.04.018.
- Brown, P. E., K. F. Kåresen, G. O. Roberts, and S. Tonellato (2000), Blur-generated non-separable space-time models, *Journal of the Royal Statistical Society Series B (Statistical Methodology)*, 62(4), 847–860, doi:10.1111/1467-9868.00269.
- Butenschön, M., and M. Zavatarelli (2012), A comparison of different versions of the SEEK filter for assimilation of biogeochemical data in numerical models of marine ecosystem dynamics, *Ocean Modelling*, 54-55, 37–54, doi:10.1016/j.ocemod.2012.06.003.
- Camps-Valls, G., L. Gómez-Chova, J. Muñoz-Marí, J. Vila-Francés, J. Amorós-López, and J. Calpe-Maravilla (2006), Retrieval of oceanic chlorophyll concentration with relevance vector machines, *Remote Sensing of Environment*, 105, 23–33, doi:10.1016/j.rse.2006.06.004.
- Ciavatta, S., R. Torres, S. Saux-Picart, and J. I. Allen (2011), Can ocean color assimilation improve biogeochemical hindcasts in shelf seas?, *Journal of Geophysical Research*, 116, C12043, doi:10.1029/2011JC007219.
- Ciavatta, S., R. Torres, V. Martínez-Vicente, T. Smyth, G. Dall'Olmo, L. Polimene, and J. I. Allen (2014), Assimilation of remotely-sensed optical properties to improve marine biogeochemistry modelling, *Progress in Oceanography*, 127, 74–95, doi:10.1016/J.Pocean.2014.06.002.
- Cressie, N., and H.-C. Huang (1999), Classes of nonseparable, spatio-temporal stationary covariance functions, *Journal of the American Statistical Association*, 94(448), 1330–1340, doi:10.1080/01621459.1999.10473885.
- Edwards, C. A., A. M. Moore, I. Hoteit, and B. D. Cornuelle (2015), Regional ocean data assimilation, *Annual Review of Marine Science*, 7, 21–42, doi:10.1146/annurev-marine-010814-015821.
- Fennel, W., and T. Neumann (2004), *Introduction to the Modelling of Marine Ecosystems*, Elsevier Oceanography Series, vol. 72, Elsevier, Amsterdam, The Netherlands.
- Fontana, C., P. Brasseur, and J.-M. Brankart (2013), Toward a multivariate re-analysis of the North Atlantic Ocean biogeochemistry during 1998–2006 based

on the assimilation of SeaWiFS chlorophyll data, *Ocean Science*, 9, 37–56, doi: 10.5194/Os-9-37-2013.

Gneiting, T. (2002), Nonseparable, stationary covariance functions for space-time data, *Journal of the American Statistical Association*, 97(458), 590–600, doi:10.1198/016214502760047113.

Gneiting, T., and P. Guttorp (2010), Continuous parameter spatio-temporal processes, in *Handbook of Spatial Statistics*, edited by A. E. Gelfand, P. J. Diggle, M. Fuentes, and P. Guttorp, Chapman & Hall/CRC Handbooks of Modern Statistical Methods, pp. 17–28, CRC Press, Boca Raton, Florida, doi:10.1201/9781420072884.

Gneiting, T., M. G. Genton, and P. Guttorp (2007), Geostatistical space-time models, stationarity, separability, and full symmetry, in *Statistical Methods for Spatio-Temporal Systems*, vol. 107, edited by B. Finkenstädt, L. Held, and V. Isham, pp. 151–175, Chapman & Hall/CRC, Boca Raton, Florida.

Gokaraju, B., S. S. Durbha, R. L. King, and N. H. Younan (2011), A machine learning based spatio-temporal data mining approach for detection of harmful algal blooms in the Gulf of Mexico, *IEEE Journal of Selected Topics in Applied Earth Observations and Remote Sensing*, 4(3), 710–720, doi:10.1109/Jstars.2010.2103927.

Hamill, T. M., and C. Snyder (2000), A hybrid ensemble Kalman filter-3D variational analysis scheme, *Monthly Weather Review*, 128, 2905–2919, doi:10.1175/1520-0493(2000)128<2905:Ahekfv>2.0.Co;2.

Handcock, M. S., and J. R. Wallis (1994), An approach to statistical spatial-temporal modeling of meteorological fields, *Journal of the American Statistical Association*, 89(426), 368–378.

Hohn, M. E., A. M. Liebhold, and L. S. Gribko (1993), Geostatistical model for forecasting spatial dynamics of defoliation caused by the Gypsy Moth (Lepidoptera: Lymantriidae), *Environmental Entomology*, 22(5), 1066–1075.

Hoteit, I., G. Korres, and G. Triantafyllou (2005), Comparison of extended and ensemble based Kalman filters with low and high resolution primitive equation ocean models, *Nonlinear Processes in Geophysics*, 12, 755–765.

James, G., D. Witten, T. Hastie, and R. Tibshirani (2013), *An Introduction to Statistical Learning: with Applications in R*, Springer, New York.

- Jeong, K. S., D. K. Kim, and G. J. Joo (2006), River phytoplankton prediction model by artificial neural network: Model performance and selection of input variables to predict time-series phytoplankton proliferations in a regulated river system, *Eco-logical Informatics*, 1, 235–245, doi:10.1016/J.Ecoinf.2006.04.001.
- Kim, Y. H., J. Im, H. K. Ha, J. K. Choi, and S. Ha (2014), Machine learning approaches to coastal water quality monitoring using GOCI satellite data, *GIScience & Remote Sensing*, 51(2), 158–174, doi:10.1080/15481603.2014.900983.
- Korres, G., G. Triantafyllou, G. Petihakis, D. E. Raitsos, I. Hoteit, A. Pollani, S. Colella, and K. Tsiaras (2012), A data assimilation tool for the Pegasitikos Gulf ecosystem dynamics: Methods and benefits, *Journal of Marine Systems*, 94, S102–S117, doi:10.1016/J.Jmarsys.2011.11.004.
- Lee, J. H. W., Y. Huang, M. Dickman, and A. W. Jayawardena (2003), Neural network modelling of coastal algal blooms, *Ecological Modelling*, 159, 179–201, doi: 10.1016/S0304-3800(02)00281-8.
- Mann, K. H., and J. R. N. Lazier (2006), *Dynamics of marine ecosystems: Biological-Physical Interactions in the Oceans (3rd edition)*, Blackwell Publishing, Malden, Maryland.
- McClain, C. R. (2009), A decade of satellite ocean color observations, *Annual Review of Marine Science*, 1, 19–42, doi:10.1146/Annurev.Marine.010908.163650.
- Miles, T. N., and R. He (2010), Temporal and spatial variability of Chl-a and SST on the South Atlantic Bight: Revisiting with cloud-free reconstructions of MODIS satellite imagery, *Continental Shelf Research*, 30, 1951–1962, doi:10.1016/j.csr.2010.08.016.
- Mulia, I. E., H. Tay, K. Roopsekhar, and P. Tkalich (2013), Hybrid ANN-GA model for predicting turbidity and chlorophyll-a concentrations, *Journal of Hydro-Environment Research*, 7, 279–299, doi:10.1016/J.Jher.2013.04.003.
- Nerger, L., W. Hiller, and J. Schröter (2005), A comparison of error subspace Kalman filters, *Tellus*, 57A(5), 715–735, doi:10.1111/J.1600-0870.2005.00141.X.
- North, G. R., J. Wang, and M. G. Genton (2011), Correlation models for temperature fields, *Journal of Climate*, 24, 5850–5862, doi:10.1175/2011jcli4199.1.

Pal, R., and A. K. Choudhury (2014), *An introduction to phytoplanktons : diversity and ecology*, Springer, New Delhi, India.

Pettersson, L. H., and D. Pozdnyakov (2013), *Monitoring of harmful algal blooms*, Springer-Praxis books in geophysical sciences, Springer, Heidelberg, Germany.

Racault, M. F., D. E. Raitsos, M. L. Berumen, R. J. Brewin, T. Platt, S. Sathyendranath, and I. Hoteit (), Phytoplankton phenology indices in coral reef ecosystems: application to ocean-colour observations in the red sea.

Raitsos, D. E., I. Hoteit, P. K. Prihartato, T. Chronis, G. Triantafyllou, and Y. Abualnaja (2011), Abrupt warming of the Red Sea, *Geophysical Research Letters*, 38, L14601, doi:10.1029/2011gl047984.

Raitsos, D. E., G. Korres, G. Triantafyllou, G. Petihakis, M. Pantazi, K. Tsiaras, and A. Pollani (2012), Assessing chlorophyll variability in relation to the environmental regime in Pagasitikos Gulf, Greece, *Journal of Marine Systems*, 94, S16–S22, doi: 10.1016/j.jmarsys.2011.11.003.

Raitsos, D. E., Y. Pradhan, R. J. W. Brewin, G. Stenchikov, and I. Hoteit (2013), Remote sensing the phytoplankton seasonal succession of the Red Sea, *PLoS One*, 8(6), e64909, doi:10.1371/journal.pone.0064909.

Raitsos, D. E., X. Yi, T. Platt, M.-F. Racault, R. J. W. Brewin, Y. Pradhan, V. P. Papadopoulos, S. Sathyendranath, and I. Hoteit (2015), Monsoon oscillations regulate fertility of the Red Sea, *Geophysical Research Letters*, 42, doi: 10.1002/2014gl062882, in press.

Richlen, M. L., S. L. Morton, E. A. Jamali, A. Rajan, and D. M. Anderson (2010), The catastrophic 2008-2009 red tide in the Arabian gulf region, with observations on the identification and phylogeny of the fish-killing dinoflagellate *Cochlodinium polykrikoides*, *Harmful Algae*, 9, 163–172, doi:10.1016/J.Hal.2009.08.013.

Robinson, I. S. (2010), *Discovering the ocean from space : the unique applications of satellite oceanography*, Springer-Praxis books on geophysical sciences, 1st ed., Springer, Heidelberg, Germany.

Shumway, B. H., and D. S. Stoffer (1982), An approach to time series smoothing and forecasting using the em algorithm, *Journal of Time Series Analysis*, 3(4).

- Sirjacobs, D., A. Alvera-Azcárate, A. Barth, G. Lacroix, Y. Park, B. Nechad, K. Rudick, and J.-M. Beckers (2011), Cloud filling of ocean colour and sea surface temperature remote sensing products over the southern north sea by the data interpolating empirical orthogonal functions methodology, *Journal of Sea Research*, *65*, 114–130, doi:10.1016/j.seares.2010.08.002.
- Stein, M. L. (2005), Space-time covariance functions, *Journal of the American Statistical Association*, *100*(469), 310–321, doi:10.1198/016214504000000854.
- Steinmetz, F., P. Y. Deschamps, and D. Ramon (2011), Atmospheric correction in presence of sun glint: application to MERIS, *Optics Express*, *19*(10), 9783–9800, doi:10.1364/Oe.19.009783.
- Tandeo, P., M. Pulido, and F. Lott (2014), Offline parameter estimation using EnKF and maximum likelihood error covariance estimates: Application to a subgrid-scale orography parametrization, *Quarterly Journal of the Royal Meteorological Society*, doi:10.1002/qj.2357.
- Taylor, M. H., M. Losch, M. Wenzel, and J. Schröter (2013), On the sensitivity of field reconstruction and prediction using empirical orthogonal functions derived from gappy data, *Journal of Climate*, *26*, 9194–9205, doi:10.1175/Jcli-D-13-00089.1.
- Tett, P., and E. D. Barton (1995), Why are there about 5000 species of phytoplankton in the sea?, *Journal of Plankton Research*, *17*(8), 1693–1704, doi:10.1093/Plankt/17.8.1693.
- Triantafyllou, G., I. Hoteit, and G. Petihakis (2003), A singular evolutive interpolated Kalman filter for efficient data assimilation in a 3-D complex physical-biogeochemical model of the Cretan Sea, *Journal of Marine Systems*, *40-41*, 213–231, doi:10.1016/S0924-7963(03)00019-8.
- Triantafyllou, G., I. Hoteit, X. Luo, K. Tsiaras, and G. Petihakis (2013), Assessing a robust ensemble-based Kalman filter for efficient ecosystem data assimilation of the Cretan Sea, *Journal of Marine Systems*, *125*, 90–100, doi:10.1016/J.Jmarsys.2012.12.006.
- Triantafyllou, G., F. Yao, G. Petihakis, K. P. Tsiaras, D. E. Raitsos, and I. Hoteit (2014), Exploring the Red Sea seasonal ecosystem functioning using a three-dimensional biophysical model, *Journal of Geophysical Research-Oceans*, *119*, 1791–1811, doi:10.1002/2013jc009641.

- Waite, J. N., and F. J. Mueter (2013), Spatial and temporal variability of chlorophyll-a concentrations in the coastal Gulf of Alaska, 1998–2011, using cloud-free reconstructions of SeaWiFS and MODIS-Aqua data, *Progress in Oceanography*, 116, 179–192, doi:10.1016/j.pocean.2013.07.006.
- Wang, H., and X. Yang (2013), Prediction and elucidation of algal dynamic variation in Gonghu Bay by using artificial neural networks and canonical correlation analysis.
- Weikert, H. (1987), Plankton and the pelagic environment, in *Red Sea*, edited by J. . E. Alasdair, pp. 90–111, Pergamon, Oxford, United Kingdom, doi:10.1016/B978-0-08-028873-4.50010-4.
- Wu, N., J. Huang, B. Schmalz, and N. Fohrer (2014), Modeling daily chlorophyll a dynamics in a German lowland river using artificial neural networks and multiple linear regression approaches, *Limnology*, 15, 47–56, doi:10.1007/S10201-013-0412-1.
- Yao, F., and I. Hoteit (2015), Thermocline regulated seasonal evolution of surface chlorophyll in the Gulf of Aden, *PLoS One*, in press.
- Yao, F., I. Hoteit, L. J. Pratt, A. S. Bower, A. Köhl, G. Gopalakrishnan, and D. Rivas (2014a), Seasonal overturning circulation in the Red Sea: 2. winter circulation, *Journal of Geophysical Research-Oceans*, 119, 2263–2289, doi:10.1002/2013jc009331.
- Yao, F., I. Hoteit, L. J. Pratt, A. S. Bower, P. Zhai, A. Köhl, and G. Gopalakrishnan (2014b), Seasonal overturning circulation in the Red Sea: 1. model validation and summer circulation, *Journal of Geophysical Research-Oceans*, 119, 2238–2262, doi:10.1002/2013jc009004.
- Zhai, P., and A. Bower (2013), The response of the red sea to a strong wind jet near the Tokar Gap in summer, *Journal of Geophysical Research-Oceans*, 118, 422–434, doi:10.1029/2012jc008444.
- Zhan, P., A. C. Subramanian, F. C. Yao, and I. Hoteit (2014), Eddies in the Red Sea: A statistical and dynamical study, *Journal of Geophysical Research-Oceans*, 119(6), 3909–3925, doi:10.1002/2013jc009563.

APPENDIX

Paper 1: Filtering remotely sensed
chlorophyll concentrations in the Red
Sea using a space-time covariance
model and a Kalman Filter

Filtering remotely sensed chlorophyll concentrations in the Red Sea using a space-time covariance model and a Kalman Filter

Denis Dreano^a, Bani Mallick^b, Ibrahim Hoteit^{a,*}

^a*Computer, Electrical and Mathematical Sciences and Engineering Division, King Abdullah University of Science and Technology*

^b*Department of Statistics, Texas A&M University*

Abstract

A statistical model is proposed to filter satellite-derived chlorophyll concentration from the Red Sea, and to predict future chlorophyll concentrations. The seasonal trend is first estimated after filling missing chlorophyll data using an Empirical Orthogonal Function (EOF)-based algorithm (Data Interpolation EOF). The anomalies are then modeled as a stationary Gaussian process. A method proposed by Gneiting [1] is used to construct positive-definite space-time covariance models for this process. After choosing an appropriate statistical model and identifying its parameters, Kriging is applied in the space-time domain to make a one step-ahead prediction of the anomalies. The latter serves as the prediction model of a reduced-order Kalman filter, which is applied to assimilate and predict future observations of chlorophyll concentrations. The proposed method decreases the root mean square

*Corresponding author

Email address: ibrahim.hoteit@kaust.edu.sa (Ibrahim Hoteit)

(RMS) prediction error by about 11% compared with the seasonal prediction.

1. Introduction

The Red Sea is an elongated basin situated between the Asian and the African shelves, connected to the Mediterranean Sea in the north through the Suez Canal, and to the Gulf of Aden in the south through the Strait of Bab el Mandeb [2]. It is one of the warmest and most saline seas in the world, with a rich ecosystem that has adapted to these extreme conditions [3]. This unique natural resource is however threatened by an abrupt increase of temperature since 1994 [4].

Phytoplankton are small, unicellular, photosynthetic algae. They are the primary producers for marine ecosystems, and at the base of the marine food chain. Phytoplankton concentration is therefore important for fisheries [5]. By fixing atmospheric CO₂ and sinking to form sediment at the bottom of the sea, phytoplankton also acts as a biological pump. This phenomenon is crucial to understanding climate change [6]. Thus modeling and predicting changes in chlorophyll concentrations have many purposes. In the Red Sea, phytoplankton is particularly important to the extensive coral reefs along its shores.

The Red Sea is generally deficient in major inorganic nutrients, and its productivity is relatively low [7, 8]. The high productivity observed in the southern Red Sea is attributed to the intrusion of nutrient-rich waters from the Gulf of Aden [7, 8]. Red Sea chlorophyll concentrations follow seasonal

22 patterns, with a winter bloom following a weak summer productivity. Con-
23 siderable interannual variability in chlorophyll concentrations has also been
24 observed [9]. However, the Red Sea ecosystem has not yet been fully ex-
25 plored, and very few in- situ measurements have been conducted in its basin
26 [10], increasing the need for remotely sensed data. Satellite observations of
27 chlorophyll concentrations have been shown to be reliable datasets to study
28 the primary productivity of the oceans [11] and they constitute the basis of
29 several studies in the Red Sea [7, 10, 9].

30 Modeling and predicting changes in phytoplankton concentrations is chal-
31 lenging. It requires the coupling of an ecological model with a hydrological
32 model, which provides the physical forcing that influences the ecology. A
33 broad range of models has been developed by the marine ecosystem research
34 community, from the simple NPZ model with only nutrients, phytoplankton
35 and zooplankton as state variables, to much more complex models. NPZ
36 models have been implemented with various degrees of success on very dif-
37 ferent regions [12]. However, there are cases when distinguishing between
38 specific groups of phytoplankton can be useful. Examples are the study
39 of export, sinking or climate feedback [12]. The European Regional Seas
40 Ecosystem Model (ERSEM) [13] is an example of a much more sophisticated
41 ecosystem model, initially designed for simulations of the North Sea. It dis-
42 tinguishes functional phytoplankton and zooplankton groups, and models the
43 complete cycling of different nutrient groups and O₂ and CO₂, and includes
44 the effect of higher trophic groups. It has recently been implemented in the

45 Red Sea [8]. Configuring ERSEM and coupling it with a physical ocean
46 model is, however, delicate and requires considerable efforts and expertise
47 [14]. A more important issue with this class of models is the number of
48 empirical equations that governs its dynamics and the number of involved
49 ecological variables and parameters (over 50 for ERSEM [15]). This makes
50 such models difficult to calibrate and validate, since there are usually not
51 enough observations to constrain the large number of parameters [12].

52 An alternative approach is to follow a statistical framework to model the
53 space-time evolution of chlorophyll concentrations. Statistical methods have
54 not been widely used in this field, which has previously relied on time-series
55 observations. Artificial neural networks were applied to forecasting algal
56 blooms in freshwater and marine systems [16, 17], and generalized additive
57 models have been use in finding explanatory variables for the chlorophyll
58 concentrations in the Pagasitikos Gulf and the subartic North Atlantic [18,
59 19].

60 Geostatistical spatio-temporal models are extensions of the spatial clas-
61 sical geostatistical methods [20]. These methods consider space-time data as
62 the realization of a Gaussian process, from which a mean and a covariance
63 function can be estimated. Although, in most applications, such a stochas-
64 tic modeling approach has no rigorous scientific basis, geostatistical methods
65 may capture some patterns in the data and avoid the difficulties of dynam-
66 ical models [21, 20]. These methods are widely employed in meteorology to
67 model the surface temperature over land and oceans [22, 23], in an ecological

68 context to study moth populations [24], and to characterize soil and pollution
69 [25, 26].

70 The first proposed spatio-temporal geostatistical model was based on sep-
71 arable covariance functions [20]. Such functions can either be the product, or
72 the sum, of a purely temporal covariance model and a purely spatial covari-
73 ance model. These covariance models are convenient but have non-physical
74 properties, limiting their use in many situations [20]. As a result, significant
75 research has been recently conducted to construct nonseparable families of
76 covariance functions. In [27, 1], the authors proposed methods to construct
77 families from known temporal and spatial covariance functions. The method
78 proposed in [1] is appealing because of its modularity and interpretability.
79 We adopte it here to model the anomaly fields of chlorophyll concentration
80 in the Red Sea.

81 Once the mean and covariance functions have been estimated from avail-
82 able satellite data after missing data have been filled with an Empirical Or-
83 thogonal Function (EOF)-based method (DINEOF [28, 29]), it is possible to
84 condition on present observations to improve the forecast of future chloro-
85 phyll concentration measurements via Kriging [20]. However, this requires
86 the inversion of the spatial observation autocovariance matrix with a 0 tem-
87 poral. In the context of remotely sensed two-dimensional (2D) fields, the
88 number of observations may be close to the number of variables. For a
89 large area and/or high resolution, this inversion can be computationally pro-
90 hibitive. Moreover, in the case of large regions of missing observations, as

91 in the southern Red Sea, the prediction will be biased at these locations
 92 [30]. This problem is tackled here by identifying the Kriging operator as
 93 an evolution matrix in a state-space context and then using a reduced-order
 94 Kalman filter [31] for the filtering and prediction of the observations. This
 95 method is computationally efficient; it implicitly uses past observations in
 96 the estimation process; and it provides a prediction of the entire state at
 97 any point in time. The reduced-order Kalman filter significantly reduces the
 98 computational burden of the traditional Kalman filter by projecting the filter
 99 covariance matrices on a fixed low-rank basis. Since the anomalies are mod-
 100 eled with a space-time Gaussian process, they are correlated in time. The
 101 formulation of the reduced-order Kalman filter is therefore expanded to take
 102 into account a colored model noise [32].

103 The paper is organized as follows. Section 2 describes the satellite data.
 104 Section 3 discusses the methodology for the data filling and geostatistical
 105 modeling. Section 4 derives the state-space formulation and introduces the
 106 space-time Kalman filtering problem and its solution. The experimental
 107 setup and numerical results are presented and discussed in section 4. Con-
 108 cluding remarks are provided in section 5.

109 **2. Data and preprocessing**

110 Satellite data provide chlorophyll (CHL) concentrations with a spatial and
 111 temporal resolution not achievable with in situ observations, making them
 112 particularly relevant to the Red Sea, where very few in situ data collection

113 are conducted.

114 Level-3 mapped data from the NASA SeaWiFS (Sea-Viewing Wide Field-
115 of-View Sensor) satellite sensor are used in this study. The dataset is publicly
116 available at <http://oceancolor.gsfc.nasa.gov>. In this study, we use the
117 9km resolution mapped weekly averages from January 1998 to December
118 2007 (460 time steps). At each time step, a 133×188 pixel map is avail-
119 able for a domain extending from longitudes between 33°E and 44°E and
120 latitudes between 12°N and 28°N , of which 5635 pixels correspond to actual
121 Red Sea surface (see Figure 1(a)). A log-transformation was applied in or-
122 der to obtain an approximately Gaussian distribution [33]. Pixels with too
123 few observations were discarded, and a control quality check was applied to
124 remove outliers [34].

125 Remotely sensed CHL may have missing data because of cloud coverage.
126 The cloud variability in the Red Sea follows a seasonal cycle. Figure 1(c)
127 shows that the cloud coverage is particularly pronounced during summers
128 because of the monsoon and it is sparse during winters. The cloud coverage
129 is, however, not homogenous over the Red Sea. It is much more pronounced
130 in the south (figure 1(b)). In this region, almost no data are available during
131 summers.

132 The dataset is separated into a training set, composed of the first seven
133 years of data, and a validation set, containing the remaining three years.
134 The computations for the data filling and for the covariance model selection
135 and estimation are based only on the training dataset. The testing dataset

₁₃₆ is used to validate the model predictions outside the training period.

₁₃₇ **3. Data filling and modeling**

₁₃₈ *3.1. Data filling*

₁₃₉ The DINEOF (Data Interpolating Empirical Orthogonal Function) is an
₁₄₀ EOF-based, recursive method for the reconstruction of data matrices with
₁₄₁ missing values [28, 29]. It estimates the values of the missing data by suc-
₁₄₂ cessive singular values decompositions (SVD) of a given data matrix and
₁₄₃ truncated reconstructions. The advantage of this method is that it does not
₁₄₄ require any a priori information about the data. It has been successfully used
₁₄₅ for reconstruction of incomplete chlorophyll datasets in different regions of
₁₄₆ the ocean [35, 36, 37].

₁₄₇ Let \mathbf{X} be an $m \times k$ centered data matrix with missing values initially filled
₁₄₈ with 0s. Then, until the missing values have converged, the following steps
₁₄₉ are repeated. An SVD is first applied to the data matrix: $\mathbf{X} = \mathbf{U}\Sigma\mathbf{V}^T$, with
₁₅₀ \mathbf{U} an $m \times m$ unitary matrix, Σ an $m \times k$ diagonal matrix and \mathbf{V} a $k \times k$ unitary
₁₅₁ matrix. The missing values are then replaced by the truncated reconstruction
₁₅₂ order n of the data matrix: $\{\mathbf{X}\}_{i,j} = \{\mathbf{U}^{(n)}\Sigma^{(n)}(\mathbf{V}^{(n)})^T\}_{i,j}$, for i, j indices
₁₅₃ of the missing values, with $\mathbf{U}^{(n)}$ the $m \times n$ matrix composed of the n first
₁₅₄ columns of \mathbf{U} , $\mathbf{V}^{(n)}$ the $k \times n$ matrix composed of the n first columns of
₁₅₅ \mathbf{V} , and $\Sigma^{(n)}$ the $n \times n$ diagonal matrix with the n largest eigenvalues on its
₁₅₆ diagonal. It is assumed that the eigenvalues and eigenvector are sorted by
₁₅₇ decreasing order of eigenvalues. In [29], the authors introduced the filtering

158 of the temporal covariance matrix as a way of reducing spurious oscillations
 159 that may appear when the data are sparsely sampled in time. This filtering
 160 is controlled by the parameter of the Laplacian filter and the number of times
 161 the filter is applied.

162 The values of the DINEOF parameters are determined following the
 163 method outlined in [29]. The smoothing parameter of the Laplacian filter
 164 is set to 0.005. The number of modes in the truncation and the number of
 165 times the filter is applied are chosen following a cross-validation technique. A
 166 random subset of observed values is taken from X and assumed to be missing
 167 before the DINEOF is applied. The algorithm is then run with different num-
 168 bers of iterations (1, 3, 10, 30, 100) and orders of truncation (from 2 to 50).
 169 The set of parameters minimizing the RMS error over the cross-validation
 170 data is chosen as the best number of iterations and order of truncation. The
 171 approach of [38] is followed to select a cross-validation dataset. Instead of
 172 selecting it by sampling the dataset point by point, contiguous regions are set
 173 aside. These regions correspond to regions of missing data from the original
 174 dataset and are selected randomly until 3% of the data have been extracted.

175 *3.2. Geostatiscal modeling*

The chlorophyll concentration data are modeled as a space-time random
 Gaussian process:

$$Z(\mathbf{s}; t), (\mathbf{s}; t) \in \mathbb{R}^2 \times \mathbb{R}. \quad (1)$$

¹⁷⁶ Such a process is entirely characterized by the mean function $\mu(\mathbf{s}; t) =$
¹⁷⁷ $E(Z(\mathbf{s}; t))$, and the covariance function $K(\mathbf{s}, \mathbf{r}; t, q) = \text{cov}(Z(\mathbf{s}; t), Z(\mathbf{r}; q))$.
¹⁷⁸ The process is further assumed to be stationary, such that the covariance
¹⁷⁹ function can be written as $K(\mathbf{s}, \mathbf{r}; t, q) = \text{cov}(Z(\mathbf{s}; t), Z(\mathbf{r}; q))$.

Covariance functions should be positive-definite, meaning that for any ensemble of space-time coordinates, $\{(\mathbf{s}_i; t_i)\}_{i=1,\dots,k}$, and real coefficients, d_1, \dots, d_k , the following condition should hold:

$$\sum_{i=1}^k \sum_{j=1}^k d_i d_j C(\mathbf{s}_i - \mathbf{s}_j; t_i - t_j) \geq 0. \quad (2)$$

¹⁸⁰ One way to enforce positive-definiteness in practice is to assume that the
¹⁸¹ covariance function belongs to a parametric family of covariance functions,
¹⁸² denoted by $C(\mathbf{h}; u|\boldsymbol{\theta})$, where $\boldsymbol{\theta}$ is the vector of parameters to be estimated
¹⁸³ [39].

¹⁸⁴ 3.3. Mean function estimation and anomalies

¹⁸⁵ The data exhibit a distinct seasonal signal accounting for roughly 50%
¹⁸⁶ of the total variability as can be seen in Figure 2. It is therefore reasonable
¹⁸⁷ to model it in the mean function $\mu(\mathbf{s}; t)$. Once the data are filled using the
¹⁸⁸ DINEOF algorithm, the seasonal signal is estimated for each week with the
¹⁸⁹ weekly average computed from the training data.

¹⁹⁰ The anomalies are then computed by subtracting the weekly averages
¹⁹¹ from the data. The CHL anomalies of the first 8 weeks of data are displayed
¹⁹² in Figure 3. There are large regions of similar colors indicating spatial corre-

193 lations. Moreover, two maps adjacent in time display similar patterns, sug-
 194 gesting that the dataset is also correlated in time and justifying the use of
 195 space-time covariance functions to model CHL anomalies. From the anomaly
 196 time-series at three locations, plotted in Figure 4, one may conclude that the
 197 data have been successfully detrended. Since no specific pattern appears, the
 198 assumption of stationarity for the covariance model seems to be appropriate.

199 *3.4. Construction and fitting of the covariance model*

200 For space-time processes, families of covariance functions are typically
 201 built by combining known spatial and temporal covariance models. Sep-
 202 arable models are the simplest example of this approach, taking the form
 203 $C(\mathbf{h}; u|\boldsymbol{\theta}) = C^1(\mathbf{h}|\boldsymbol{\theta}_1)C^2(t|\boldsymbol{\theta}_2)$, where C^1 and C^2 are respectively pure spa-
 204 tial and temporal covariance models parametrized by $\boldsymbol{\theta}_1$ and $\boldsymbol{\theta}_2$. However,
 205 realizations from such families of covariance models were shown to exhibit
 206 non-physical behaviors [1, 27]. Research has been conducted to develop meth-
 207 ods for constructing non-separable covariance functions to overcome these
 208 limitations [27, 1].

In this work, families of space-time covariance functions are constructed
 following an approach proposed by Gneiting [1]. Given any completely
 monotonous function, $\varphi(t), t \geq 0$, and any positive function with a com-
 pletely monotonous derivative, $\psi(t), t \geq 0$, the following space-time covari-

ance function is valid (i.e., positive-definite):

$$C(\mathbf{h}; u) = \frac{\sigma^2}{\psi(|u|^2)} \varphi \left(\frac{||\mathbf{h}||^2}{\psi(|u|^2)} \right), (\mathbf{h}, u) \in \mathbb{R}^2 \times \mathbb{R}. \quad (3)$$

- 209 In general, φ is defined as a temporal covariance function, and ψ as a spatial
 210 covariance model, e.g., the exponential model or the Matérn model. Tables 1
 211 and 2 present some examples of these functions that were introduced in [1].
 212 To obtain more specialized families, a nugget term can be added.

The typical approach for estimating the parameters of the covariance function is by fitting it to the empirical space-time covariance matrix [39].

The empirical covariance function is first estimated using the formula:

$$2\hat{C}(\mathbf{h}(l); u) = \frac{1}{|N(\mathbf{h}(l); u)|} \sum_{(i,j,t,t') \in N(\mathbf{h}(l); u)} a(\mathbf{s}_i; t)a(\mathbf{s}_j; t'), \quad (4)$$

with $N(\mathbf{h}(l); u) = \{(i, j, t, t') \text{ such that } : |t - t'| = u, \mathbf{s}_i - \mathbf{s}_j \in \text{Bin}(\mathbf{h}(l))\}$, where \mathbb{R}^2 has been divided into a finite number of bins, $\text{Bin}(\mathbf{h}(l))$, each of which has a representative lag, $\mathbf{h}(l)$. Here, bins are considered of the form $\mathbf{k} \in \text{Bin}(\mathbf{h}(l))$ if $(l - 1) * \delta h \leq ||\mathbf{k}|| \leq l\delta h, l = 0, \dots, L$, with δ a fixed interval size and L the number of retained intervals. The parameters are then estimated by fitting the covariance model using the Weighted Least Squares (WLS) approach. This method is popular due to its simplicity and proven efficiency [40]. In practice, the estimator of $\boldsymbol{\theta}$ minimizes the weighted sum of the squares of

errors:

$$S(\boldsymbol{\theta}) = \sum_l \sum_{u=0}^3 w_{l,u} \left(\hat{C}(\mathbf{h}(l); u) - C(\mathbf{h}(l); u|\boldsymbol{\theta}) \right)^2, \quad (5)$$

213 with weights $w_{l,u} = \frac{|N(\mathbf{h}(l); u)|}{(1-C(\mathbf{h}(l); u|\boldsymbol{\theta}))^2}$. ϕ and ψ are chosen from the functions
 214 presented in Tables 1 and 2, by separately fitting the covariance function in
 215 time and space for all possible choices of ϕ and ψ . The choice of the functions
 216 is then made based on the quality of the fit.

217 4. State-space formulation and filtering

218 So far, the CHL data are modeled as $Z(\mathbf{s}; t) = \mu(\mathbf{s}; t) + a(\mathbf{s}; t)$, where μ
 219 is a deterministic function representing the seasonality and a is a zero-mean
 220 space-time Gaussian process representing the weekly anomalies, with the
 221 covariance function estimated as described in the previous section. However,
 222 a state-space model needs to be formulated to use the Kalman filter. This
 223 is done by identifying a CHL underlying process, $Y(\mathbf{s}; t)$, distinct from the
 224 data process $Z(\mathbf{s}; t)$. These processes are then discretized in space and time
 225 to obtain the state-space formulation, on which a reduced-order variant of
 226 the Kalman filter is applied.

²²⁷ 4.1. State-space modeling

To derive the state-space model, we start from the following model:

$$Y(\mathbf{s}; t) = \mu(\mathbf{s}; t) + a(\mathbf{s}; t), \text{ where } \mathbf{s}, t \text{ are observable,} \quad (6)$$

$$Z(\mathbf{s}; t) = Y(\mathbf{s}; t) + \varepsilon(\mathbf{s}; t), \text{ where } \mathbf{s}, t \text{ are observed.} \quad (7)$$

²²⁸ In this formulation, $\varepsilon(\mathbf{s}; t)$ is a white noise process representing the mea-
²²⁹ surement errors, $a(\mathbf{s}; t)$ is the anomaly process with the covariance matrix
²³⁰ estimated as described in the previous section, $\mu(\mathbf{s}; t)$ is the seasonal mean
²³¹ function, $Y(\mathbf{s}; t)$ is the underlying CHL log-concentration process, and $Z(\mathbf{s}; t)$
²³² the data process.

To build a state-space model for filtering and forecasting the spatial variability of CHL in time, once the covariance function is estimated, we resort to Kriging. In classical geostatistics, Kriging interpolates available observations to provide the best linear unbiased estimate of a spatial process at unobserved locations [39]. This technique easily generalizes to space-time Gaussian processes, particularly for forecasting. The equations are obtained by conditioning the anomalies at time t by the anomalies at time $t - 1$. Using the vectorial notations $\mathbf{a}_t = \{a(\mathbf{s}_{i,t})\}_{i=1,\dots,k}$, where $\mathbf{s}_{i,t}$ is the spatial location of the i -th observation at time t , $[\mathbf{a}_t^T, \mathbf{a}_{t-1}^T]^T$ is a Gaussian vector. Therefore,

by conditioning

$$\mathbf{a}_t | \mathbf{a}_{t-1} \sim N(\mathbf{M}\mathbf{a}_{t-1}, \mathbf{Q}), \quad (8)$$

$$(9)$$

where

$$\mathbf{M} = \mathbf{C}_1 \mathbf{C}_0^{-1}, \quad (10)$$

$$\mathbf{Q} = \mathbf{C}_0 - \mathbf{C}_1 \mathbf{C}_0^{-1} \mathbf{C}_1, \quad (11)$$

with $\mathbf{C}_0 = E[\mathbf{a}_t \mathbf{a}_t^T] = \{C(\mathbf{s}_{i,t} - \mathbf{s}_{j,t}), 0\}_{i,j=1,\dots,k}$ and $\mathbf{C}_1 = E[\mathbf{a}_t \mathbf{a}_{t-1}^T] = \{C(\mathbf{s}_{i,t} - \mathbf{s}_{j,t-1}), 1\}_{i,j=1,\dots,k}$, the following recursive state-space model can be derived:

$$\mathbf{y}_t = \boldsymbol{\mu}_t + \mathbf{M}(\mathbf{y}_{t-1} - \boldsymbol{\mu}_{t-1}) + \boldsymbol{\eta}_t, \quad (12)$$

$$\mathbf{z}_t = \mathbf{H}_t \mathbf{y}_t + \boldsymbol{\varepsilon}_t, \quad (13)$$

and $\mathbf{y}_t = \mathbf{a}_t + \boldsymbol{\mu}_t$ is the CHL process discretized in space, $\boldsymbol{\mu}_t$ is the vector seasonal component, H_t is the observation operator that returns the CHL concentration at the observed location, $\boldsymbol{\eta}_t$ represents the model error, and $\boldsymbol{\varepsilon}_t$ represents the measurement error. \mathbf{y}_t is a vector of fixed size that represents the whole model domain (Red Sea), whereas \mathbf{z}_t has a variable size equal to the number of available observations at time t .

The model can be reformulated such that only the anomalies are filtered

and a_t is the state vector:

$$\mathbf{a}_t = \mathbf{M}\mathbf{a}_{t-1} + \boldsymbol{\eta}_t, \quad (14)$$

$$\mathbf{z}_t = \mathbf{y}_t - \mathbf{H}_t \mathbf{s}_t = \mathbf{H}_t \mathbf{a}_t + \boldsymbol{\varepsilon}_t. \quad (15)$$

This system is equivalent to the preceding one, but is more practical to implement. Given $\boldsymbol{\eta}_t \sim N(0, \mathbf{Q})$ and assuming $\boldsymbol{\varepsilon}_t \sim N(0, \sigma_{\text{obs}}^2 \mathbf{I})$, independent and identically distributed (i.i.d.), with σ_{obs}^2 a fixed constant that is tuned by minimizing the RMS prediction error.

4.2. Low-rank Kalman filter

Two issues need to be tackled before using the time evolution model for predicting the anomalies. First, the consequent amount of missing data in the CHL satellite observations makes it difficult to obtain frequent initial CHL concentrations to integrate the model forward in time for forecasting, and second, the model is linear with eigenvalues smaller than one¹ in absolute values, making it inappropriate for long-term predictions. The latter means that CHL model forecasts would decrease exponentially in time, quickly becoming close to 0. The Kalman filter solves both problems by recursively assimilating the observations and providing an optimal estimate, in the mean-square sense, of the anomalies to start a new forecast cycle. The filter operates in two steps to compute the best linear estimate of the state

¹This was verified numerically in the present work. We are not aware of a general result.

255 of a linear dynamical model given past observations [41].

- *Forecast step:* Starting from the best available estimate of the state, a_{t-1}^a , and the associated error covariance matrix, P_{t-1}^a , at a given time, $t - 1$, the forecast state, a_t^f , and its error covariance matrix, P_t^f , are obtained by integrating the model forward to the time of the next available observation:

$$\mathbf{a}_t^f = \mathbf{M}\mathbf{a}_{t-1}^a, \quad (16)$$

$$\mathbf{P}_t^f = \mathbf{M}\mathbf{P}_{t-1}^a\mathbf{M}^T + \mathbf{Q}. \quad (17)$$

- *Update step:* Once a new observation, \mathbf{z}_t , is available, the forecast state, \mathbf{a}_t^f , and its error covariance, \mathbf{P}_t^f , are updated to their analysis counterparts, \mathbf{a}_t^a , and, \mathbf{P}_t^a , as:

$$\mathbf{a}_t^a = \mathbf{a}_t^f + \mathbf{K}_t(\mathbf{z}_t - \mathbf{H}_t\mathbf{a}_t^f), \quad (18)$$

$$\mathbf{P}_t^a = (\mathbf{I} - \mathbf{K}_t\mathbf{H}_t)\mathbf{P}_t^f, \quad (19)$$

$$\mathbf{K}_t = \mathbf{P}_t^f\mathbf{H}_t^T(\mathbf{H}_t\mathbf{P}_t^f\mathbf{H}_t^T + \sigma_{\text{obs}}^2\mathbf{I})^{-1} \quad (20)$$

256 where K_t is known as the Kalman gain.

The inversion in the computation of the Kalman gain is computationally quite demanding because the number of observations is as large as the size of the state. To speed up this computation, the reduced-order Kalman filter [31]

is used. This filter approximates the covariance matrices as $\mathbf{P}_t^f = \mathbf{L}\mathbf{U}_t^f\mathbf{L}^T$ and $\mathbf{P}_t^a = \mathbf{L}\mathbf{U}_t^a\mathbf{L}^T$, where \mathbf{L} is a $n \times r$ matrix whose columns are the r leading EOFs (computed here with the DINEOF algorithm), and \mathbf{U}_t^f and \mathbf{U}_t^a are $r \times r$ matrices. The inversion is then applied on the $r \times r$ matrices \mathbf{U}_t^f and \mathbf{U}_t^a , which considerably reduces the computational burden since $r \ll n$ in practice [31]. Defining

$$\mathbf{V} = \mathbf{L}^T \mathbf{Q} \mathbf{L}, \quad (21)$$

$$\mathbf{W} = \mathbf{L}^T \mathbf{M} \mathbf{L}, \quad (22)$$

which respectively represent the projection of the model dynamics and the model error on the leading EOFs, the reduced-order Kalman filter equations for the forecast and update of the covariance matrix can be simplified by only updating \mathbf{U}_t^f and \mathbf{U}_t^a as follows:

$$\mathbf{U}_t^f = \mathbf{W} \mathbf{U}_{t-1}^a \mathbf{W}^T + \mathbf{V}, \quad (23)$$

$$(\mathbf{U}_t^a)^{-1} = (\mathbf{U}_t^f)^{-1} + \mathbf{L}^T \mathbf{H}^T \mathbf{R}^{-1} \mathbf{H} \mathbf{L}. \quad (24)$$

The Kalman gain can be then computed as

$$\mathbf{K}_t = \sigma_{\text{obs}}^{-2} \mathbf{L} \mathbf{U}_t^a \mathbf{L}^T \mathbf{H}^T. \quad (25)$$

257 Otherwise, the forecast and update steps are identical to those of the Kalman
 258 filter.

259 4.3. Low-rank Kalman filter with colored noise

260 One issue is that the model noise is correlated in time, whereas the
261 Kalman filter assumes it to be white. Indeed, $\boldsymbol{\eta}_t = \mathbf{a}_t - \mathbf{M}\mathbf{a}_{t-1}$ is a space-
262 time Gaussian process. One can show that $[\boldsymbol{\eta}_t^T, \boldsymbol{\eta}_{t-1}^T]^T$ is a Gaussian vector
263 of mean 0 and covariance matrix $\begin{bmatrix} \mathbf{A}_0 & \mathbf{A}_1 \\ \mathbf{A}_1^T & \mathbf{A}_0 \end{bmatrix}$, with $\mathbf{A}_0 = \mathbf{C}_0 - \mathbf{C}_1\mathbf{C}_0^{-1}\mathbf{C}_1^T$,
264 $\mathbf{A}_1 = \mathbf{C}_1\mathbf{C}_0^{-1}\mathbf{C}_1\mathbf{C}_0^{-1}\mathbf{C}_1 - \mathbf{C}_2\mathbf{C}_0^{-1}\mathbf{C}_1$. We can then predict $\boldsymbol{\eta}_t$ by condition-
265 ing on the previous equation and derive the model $\boldsymbol{\eta}_t = \mathbf{N}\boldsymbol{\eta}_{t-1} + \boldsymbol{\xi}_t$, with
266 $\mathbf{N} = \mathbf{A}_1\mathbf{A}_0^{-1}$ and $\boldsymbol{\xi}_t \sim \mathcal{N}(0, \mathbf{A}_0 - \mathbf{A}_1\mathbf{A}_0^{-1}\mathbf{A}_1)$.

267 To take into account this correlation in the Kalman filter, the state-space
268 system is enlarged by including $\boldsymbol{\eta}_t$ in the state vector [32], so the new state-
269 space system becomes:

$$\hat{\mathbf{a}}_t = \boldsymbol{\Gamma}\hat{\mathbf{a}}_{t-1} + \hat{\boldsymbol{\eta}}_t, \quad (26)$$

$$\mathbf{y}_t = \hat{\mathbf{H}}\hat{\mathbf{a}}_{t-1} + \boldsymbol{\varepsilon}_t, \quad (27)$$

270 with $\hat{\mathbf{a}}_t = [\mathbf{a}_t^T, \boldsymbol{\eta}_t^T]^T$, $\boldsymbol{\Gamma} = \begin{bmatrix} \mathbf{M} & \mathbf{I} \\ \mathbf{0} & \mathbf{N} \end{bmatrix}$, $\hat{\boldsymbol{\eta}}_t = [\mathbf{0}, \boldsymbol{\xi}_t^T]^T$ and $\hat{\mathbf{H}}_t = [\mathbf{H}_t, \mathbf{0}]$, on
271 which the Kalman filter is applied. Of course, $\boldsymbol{\xi}_t$ is again colored, but the
272 procedure can be iterated until no significant correlation is left to exploit in
273 the noise.

²⁷⁴ **5. Results**

²⁷⁵ Figure 5 summarizes the workflow of the experimental setup. The chloro-
²⁷⁶ phyll concentration is the sum of a seasonal component and an anomaly. The
²⁷⁷ former is estimated using data filled by the DINEOF algorithm over a learn-
²⁷⁸ ing period (first seven years of CHL data). The anomalies are assumed to be
²⁷⁹ a stationary Gaussian process whose space-time covariance matrix has been
²⁸⁰ estimated. A reduced-order Kalman filter is then applied to perform one-
²⁸¹ step ahead predictions. These are compared with the observations over the
²⁸² remaining three years of validation data to validate the system's performance
²⁸³ and results. The results of the DINEOF data filling algorithm are presented
²⁸⁴ before a covariance model for the data is chosen and fitted. The results of
²⁸⁵ the filtering are finally examined and analyzed.

²⁸⁶ *5.1. DINEOF Analysis*

²⁸⁷ Figure 6 plots the (RMS) error for the cross-validation dataset and for
²⁸⁸ different values of the number of smoothing iterations and EOFs. A lower
²⁸⁹ RMS error is achieved with 24 EOFs and 30 iterations.

²⁹⁰ Figures 7(a) and 7(c) show the first spatial and associated temporal modes
²⁹¹ resulting from the DINEOF analysis. Figure 7(c) exhibits a regular peak dur-
²⁹² ing winters and a secondary peak of varying size during summers. These can
²⁹³ be associated with the winter bloom and the secondary summer bloom, both
²⁹⁴ described in [9]. Figure 7(a) shows that the bloom is relatively homoge-
²⁹⁵ neous over the Red Sea, except in the southwest corner where the variation

296 is strongly pronounced.

297 Figures 7(b) and 7(d) plot the second spatial and temporal modes re-
298 spectively. The spatial mode shows a north-south contrast. The time series
299 displays a large peak around summer 2000, which corresponds to a large
300 positive anomaly taking place during this period (Figure 7(e)). Except for
301 the first two modes, all other modes tend to explain a local feature of the
302 data. This makes the interpretation of the EOF analysis difficult and the
303 convergence of the spectrum very slow as shown in Figure 7(f).

304 *5.2. Covariance model estimation*

305 Figure 8a plots the empirical space covariance function $\hat{C}(\|\mathbf{h}\|, 0)$. Among
306 the functions in Table 1, the ones that best fit this curve are selected. A WLS
307 minimization is applied to fit the parameters c , γ and ν , as well as a the noise
308 variance $\sigma_{\text{spatial}}^2$ while ignoring the observations for $\|\mathbf{h}\| = 0$. This allows a
309 nugget effect to be taken account. The results are superimposed on Figure
310 8a. The Matérn model clearly fits poorly. By examining the residuals, we
311 can obviously eliminate φ_4 . Finally, between the two remaining candidates,
312 both of which appear to be plausible, φ_1 is chosen since it involves fewer
313 degrees of freedom.

314 Figure 8b plots the empirical time covariance function $\hat{C}(0; u)$. ψ_2 defines
315 a time covariance that decreases very slowly. The covariance with ψ_3 con-
316 verges to a constant as the time-lag goes to infinity, which is not realistic in
317 the case of anomalies. The first-time covariance model is filled with a nugget

³¹⁸ effect for $u = 0$, using WLS, and the result is displayed in Figure 8b, where
³¹⁹ a nugget effect can be clearly identified.

To build the space-time covariance function, we use the reparametrization in [1] (see example 1), along with the building blocks in time and space that have been derived in Section 3. A time-only nugget effect is also added, leading to the following covariance model:

$$C(\mathbf{h}; u) = \begin{cases} \sigma^2 \exp(-c||\mathbf{h}||^{2\gamma}) & , \text{ if } u = 0, \\ \frac{\sigma^2 \tau}{a|u|^{2\alpha} + 1} \exp\left(-\frac{c||\mathbf{h}||^{2\gamma}}{(a|u|^{2\alpha} + 1)^{\beta\gamma}}\right) & , \text{ otherwise,} \end{cases} \quad (28)$$

³²⁰ with $0 < \tau \leq 1$.

³²¹ The initial values for the WLS fitting are given by the results of the
³²² preceding purely spatial and purely temporal regressions. The results are
³²³ shown in Table 3. A contour plot of the resulting covariance function is
³²⁴ shown in Figure 9. Our fitted correlation model has level curves very close
³²⁵ to those of the empirical covariance model.

³²⁶ 5.3. Filtering

³²⁷ σ_{obs}^2 is first determined empirically by trial and error, chosen as the value
³²⁸ that leads to the minimal averaged RMS error (RMSE). $\sigma_{\text{obs}}^2 = 1$ is found to
³²⁹ be a reasonable choice.

³³⁰ The anomaly model with a space-time covariance function helps to de-
³³¹ crease the RMS error by nearly 11% over the test period. As Figure 10a indi-
³³² cates, the improvement is most noticeable during periods with large anomalies.

333 The boxplot in Figure 10b shows that the variability of errors is reduced with
 334 the proposed filtering approach. Since the modeling is purely statistical and
 335 is not based on physical quantities, it was not able to anticipate the start
 336 of a bloom. However, it successfully extrapolates the current estimate of
 337 the anomaly in space and time and improves the prediction compared to the
 338 seasonal component.

339 In Figures 11 (a to c), the predictions of the model are compared with
 340 the observations and the seasonal signal for a fall week in 2006. The model
 341 captures some differences with the seasonal regime, such as a larger northern
 342 region with a low CHL concentration extending south below 22°N, and a
 343 more intense bloom in the south. The usual seasonal dynamic is altered with
 344 an extension of the stratified regime in the north and a larger intrusion of
 345 the nutrient rich waters of the Gulf of Aden [9].

346 Figure 11 (d to f) shows a similar comparison for a winter week in 2006.
 347 The model captures a weak winter bloom in the northern half of the Red
 348 Sea. A similar pattern has been described in [7] for winter 1999, and it
 349 seems to be a common feature of El Niña years. The model also successfully
 350 captures a high CHL concentration in the south, and a lower than usual CHL
 351 concentration in the center [9].

352 Figure 12 plots the error variance as predicted by the filter and the actual
 353 prediction RMSE, computed as the difference between the model forecast
 354 and data, averaged over the three year training period at every point of the
 355 grid. The predicted RMSE corresponds to the diagonals of the prediction

covariance matrix as estimated by the reduced-order Kalman filter. The prediction RMSE is computed from the error between the model prediction and the observation. We can see that both values are close in the northern half of the Red Sea, but the RMSE is much larger in the south. This is caused by the lack of data and the fact that the dynamics in the South is different from that in the north, making the process nonstationary. Indeed, as shown in Figure 3, the anomalies in the south clearly exhibit smaller spatial and temporal correlation length scales compared with those in the north.

One way to evaluate the filter's behavior is to examine the distribution of the innovations and the increments [42]. The innovation corresponds to the difference: $\mathbf{y}_t - \mathbf{H}_t \mathbf{a}_t^f$, whereas the increment corresponds to the difference: $\mathbf{H}_t (\mathbf{a}_t^a - \mathbf{a}_t^f)$. Figure 13(c) shows that the innovation seems to be approximately normally distributed, as expected for a properly tuned Kalman filter. Figure 13(b) shows that the averaged innovation size decreases to a value close to zero as the filter assimilates the data over time, which also suggests that the filter is properly working. However, Figure 13(a) indicates that the increments of the filter tend to be positively biased in some regions. This indicates that the model tends to underestimate the amount of CHL, which may be associated with the statistical model's inability to forecast CHL blooms.

Figures 14 (a), (b) and (c) plot the spatially averaged correlations between the observations and the seasonal predictions, the Kalman filter forecasts and the analyses, respectively. Compared with the seasonal correlations, we can see that the model improves the prediction skill over the entire Red Sea,

379 particularly in its central part, with correlations ranging between 0.28 and
 380 0.92. The filter further improves the prediction-data correlation, over the
 381 entire domain with correlations up to 0.96.

382 **6. Discussion**

383 Here, we considered the filtering problem of satellite-derived chlorophyll
 384 (CHL) concentration in the Red Sea using a data-driven approach in which
 385 the CHL spatio-temporal evolution is modeled as a space-time Gaussian pro-
 386 cess. The DINEOF data-filling algorithm [38] was applied to compute an
 387 estimate of the seasonal signal in the data, which was used as the mean
 388 function of the process. To model the residual anomalies, the method pro-
 389 posed by Gneiting in [1] was applied to construct an appropriate family of
 390 covariance functions.

391 From the anomalies, a family of covariance functions is constructed and
 392 then fitted to the data. Based on a space-time Kriging formulation, a linear
 393 model was derived to capture changes in the chlorophyll concentration. A
 394 reduced-order variant of the Kalman filter was then applied to forecast and
 395 filter the CHL concentration. The results of our experiments suggest that
 396 the proposed system works reasonably well, reducing the RMS error in CHL
 397 concentration prediction by about 11% as compared with the seasonal mean.

398 The proposed approach is not difficult to apply, but requires some coding

efforts. For the DINEOF, a standalone package is freely available online². To the authors' knowledge, there is currently no R package or library for fitting custom space-time covariance models. The reduced-order Kalman filter is straightforward to implement.

The proposed method requires the estimation of a very few parameters, which may prevent overfitting. Another advantage is its stability, as the anomaly prediction cannot grow over time. One problem with Kriging is that in the case of missing data over large areas, its prediction will be the mean function [30]. In this study, this problem is alleviated using the Kalman filter which always provides a prediction over the whole domain.

Forecasting and filtering CHL concentration in the Red Sea using remotely sensed data is challenging. Because of cloud coverage over the southern Red Sea during the summer, large areas remain unobserved. Moreover, the Red Sea is a heterogenous environment with different ecological and physical dynamics from north to south. We can therefore expect the anomalies to be non-stationary. Fortunately, Kriging is robust to non-stationarity [30]. A problem with this correlation-based modeling is its inability to forecast CHL blooms. Our linear model tends to underestimate the amount of CHL concentration and to miss blooms in some regions, before the Kalman filter corrects this error when new observations are available.

The proposed method can be further generalized by considering more

²<http://modb.oce.ulg.ac.be/mediawiki/index.php/DINEOF>

420 sophisticated mean functions. For example, one can use a linear model with
 421 additional covariates, such as sea surface temperature, sea surface height,
 422 thermocline depth or wind speed. Another way to improve the model is to
 423 use non-stationary covariance functions, or to use non-Gaussian models to
 424 predict blooms. These tasks will be considered in future studies.

425 **Acknowledgment**

426 The research reported in this publication was supported by King Abdullah
 427 University of Science and Technology (KAUST).

428 **7. Bibliography**

- 429 [1] T. Gneiting, Nonseparable, Stationary Covariance Functions for Space-
 430 Time Data, *Journal of the American Statistical Association* 97 (458)
 431 (2002) 590–600. doi:10.1198/016214502760047113.
- 432 [2] F. Yao, I. Hoteit, L. J. Pratt, A. S. Bower, P. Zhai, A. Köhl, G. Gopalakrishnan, Seasonal overturning circulation in the Red Sea: part 1. Model validation and summer circulation, *Journal of Geophysical Research: Oceans* (2014) 2238–2262doi:10.1002/2013JC009331.Key.
- 433 [3] S. Heileman, N. Mistafa, III-6 Red Sea: LME# 33, lme.noaa.gov.
 434 URL http://www.lme.noaa.gov/lmeweb/LME_Report/lme_33.pdf
- 435 [4] D. E. Raitsos, I. Hoteit, P. K. Prihartato, T. Chronis, G. Triantafyllou,

- 439 Y. Abualnaja, Abrupt warming of the Red Sea, Geophysical Research
 440 Letters 38. doi:10.1029/2011GL047984.
- 441 [5] A. Lo-Yat, S. D. Simpson, M. Meekan, D. Lecchini, E. Martinez,
 442 R. Galzin, Extreme climatic events reduce ocean productivity and
 443 larval supply in a tropical reef ecosystem, Global Change Biology 17
 444 (2011) 1695–1702. doi:10.1111/j.1365-2486.2010.02355.x.
 445 URL <http://onlinelibrary.wiley.com/doi/10.1111/j.1365-2486.2010.02355.x/full>
- 446 [6] K. H. Mann, J. R. N. Lazier, Dynamics of Marine Ecosystems, 2006.
- 447 [7] J. Acker, G. Leptoukh, S. Shen, T. Zhu, S. Kempler, Remotely-sensed
 448 chlorophyll a observations of the northern Red Sea indicate seasonal
 449 variability and influence of coastal reefs, Journal of Marine Systems 69
 450 (2008) 191–204. doi:10.1016/j.jmarsys.2005.12.006.
 451 URL <http://linkinghub.elsevier.com/retrieve/pii/S0924796307000589>
- 452 [8] G. Triantafyllou, F. Yao, G. Petihakis, K. Tsiaras, D. E. Raitsos,
 453 I. Hoteit, Exploring the Red Sea seasonal ecosystem functioning using a
 454 three-dimensional biophysical model, Journal of Geophysical Research:
 455 Oceans (2014) 1791–1811doi:10.1002/2013JC009641.Received.
- 456 [9] D. E. Raitsos, Y. Pradhan, R. J. W. Brewin, G. Stenchikov, I. Hoteit,
 457 Remote Sensing the Phytoplankton Seasonal Succession of the Red Sea,
 458 PLoS ONE 8 (6). doi:10.1371/journal.pone.0064909.

- 459 [10] R. J. W. Brewin, D. E. Raitsos, Y. Pradhan, I. Hoteit, Comparison
 460 of chlorophyll in the Red Sea derived from MODIS-Aqua and in
 461 vivo fluorescence, *Remote Sensing of Environment* 136 (2013) 218–224.
 462 doi:10.1016/j.rse.2013.04.018.
- 463 URL <http://dx.doi.org/10.1016/j.rse.2013.04.018>
- 464 [11] C. R. McClain, A Decade of Satellite Ocean Color Ob-
 465 servations, *Annual Review of Marine Science* (2009) 19–
 466 42doi:10.1146/annurev.marine.010908.163650.
- 467 [12] T. R. Anderson, Plankton functional type modelling: running
 468 before we can walk?, *Journal of Plankton Research* 27 (11).
 469 doi:10.1093/plankt/fbi076.
- 470 URL <http://www.plankt.oxfordjournals.org/cgi/doi/10.1093/plankt/fbi076>
- 471 [13] J. Baretta, W. Ebenhöh, P. Ruardij, The European regional seas
 472 ecosystem model, a complex marine ecosystem model, *Netherlands*
 473 *Journal of Sea Research* 33 (3/4) (1995) 233–246. doi:10.1016/0077-
 474 7579(95)90047-0.
- 475 URL <http://linkinghub.elsevier.com/retrieve/pii/0077757995900470>
- 476 [14] G. Petihakis, G. Triantafyllou, I. J. Allen, I. Hoteit, C. Dounas, Mod-
 477 elling the spatial and temporal variability of the Cretan Sea ecosystem,
 478 *Journal of Marine Systems* 36 (2002) 173–196.
- 479 [15] J. C. Blackford, P. J. Radford, A Structure and methodology for ma-

- 480 marine ecosystem modelling, Netherlands Journal of Sea Research 33 (3/4)
481 (1995) 247–260.

482 [16] J. H. W. Lee, Y. Huang, M. Dickman, A. W. Jayawardena, Neural
483 network modelling of coastal algal blooms 159 (2003) 179–201.

484 [17] F. Recknagel, Artificial neural network approach for modelling and pre-
485 diction of algal blooms, Ecological Modelling 96 (1997) 11–28.

486 [18] D. Raitsos, G. Korres, G. Triantafyllou, G. Petihakis, M. Pantazi,
487 K. Tsiaras, A. Pollani, Assessing chlorophyll variability in relation
488 to the environmental regime in Pagasitikos Gulf, Greece, Journal of
489 Marine Systems 94 (2012) S16–S22. doi:10.1016/j.jmarsys.2011.11.003.
490 URL <http://linkinghub.elsevier.com/retrieve/pii/S0924796311002703>

491 [19] D. E. Raitsos, S. J. Lavender, Y. Pradhan, T. Tyrrell, P. C. Reid, M. Ed-
492 wards, Coccolithophore bloom size variation in response to the regional
493 environment of the subarctic North Atlantic, Limnology and Oceanog-
494 raphy 51 (5) (2006) 2122–2130. doi:10.4319/lo.2006.51.5.2122.
495 URL http://www.aslo.org/lo/toc/vol_51/issue_5/2122.html

496 [20] P. C. Kyriakidis, A. G. Journel, Geostatistical Space-Time Models: A
497 Review, Mathematical Geology 31 (6) (1999) 651–684.

498 [21] N. Cressie, C. K. Wikle, Statistics for Spatio-Temporal Data, 2011.

499 [22] M. S. Handcock, J. R. Wallis, An Approach to Statistical Spatial-

- 500 Temporal Modeling of Meteorological Fields, *Journal of the American*
 501 Statistical Association
- 89 (426) (1994) 368–378.
- 502 [23] G. R. North, J. Wang, M. G. Genton, Correlation Models for
 503 Temperature Fields, *Journal of Climate* 24 (2011) 5850–5862.
 504 doi:10.1175/2011JCLI4199.1.
- 505 [24] M. E. Hohn, A. M. Liebhold, L. S. Gribko, Geostatistical Model for
 506 Forecasting Spatial Dynamics of Defoliation Caused by the Gypsy Moth
 507 (Lepidoptera: Lymantriidae), *Environmental Entomology* 22 (5) (1993)
 508 1066–1075.
- 509 [25] R. Lark, Towards soil geostatistics, *Spatial Statistics* 1 (2012) 92–99.
- 510 [26] A. Keaney, J. McKinley, C. Graham, M. Robinson, A. Ruffell, Spatial
 511 statistics to estimate peat thickness using airborne radiometric data,
 512 *Spatial Statistics* 5 (2013) 3–24.
- 513 [27] N. Cressie, H.-C. Huang, Classes of Nonseparable, Spatio-Temporal Sta-
 514 tionary Covariance Functions, *Journal of the American Statistical As-
 515 sociation* 94 (448) (1999) 1330–1340.
- 516 [28] J.-M. Beckers, M. Rixen, EOF Calculations and Data Filling from In-
 517 complete Oceanographic Datasets, *Journal of Atmospheric and Oceanic
 518 Technology* 20 (2003) 1839–1856.
- 519 [29] A. Alvera-Azcárate, A. Barth, D. Sirjacobs, J.-M. Beckers, Enhancing

- 520 temporal correlations in EOF expansions for the reconstruction of miss-
- 521 ing data using DINEOF, *Ocean Science* 5 (2009) 475–485.
- 522 [30] P. Monestiez, L. Dubroca, E. Bonnin, J.-P. Durbec, C. Guinet, Geo-
- 523 statistical modelling of spatial distribution of *Balaenoptera physalus*
- 524 in the Northwestern Mediterranean Sea from sparse count data and
- 525 heterogeneous observation efforts, *Ecological Modelling* 193 (3-4) (2006)
- 526 615–628. doi:10.1016/j.ecolmodel.2005.08.042.
- 527 URL <http://linkinghub.elsevier.com/retrieve/pii/S0304380005004436>
- 528 [31] I. Hoteit, D.-T. Pham, J. Blum, A simplified reduced order Kalman fil-
- 529 tering and application to altimetric data assimilation in Tropical Pacific,
- 530 *Journal of Marine Systems* 36 (2002) 101–127.
- 531 [32] C. K. Chui, G. Chen, *Kalman Filtering, with Real-Time Applications*,
- 532 Fourth Edition, 2009.
- 533 [33] J. W. Campbell, The lognormal distribution as a model for bio-optical
- 534 variability in the sea, *Journal of Geophysical Research* 100 (13) (1995)
- 535 237–254.
- 536 [34] J. K. Willis, Interannual variability in upper ocean heat content, tem-
- 537 perature, and thermosteric expansion on global scales, *Journal of Geo-*
- 538 *physical Research* 109. doi:10.1029/2003JC002260.
- 539 URL <http://doi.wiley.com/10.1029/2003JC002260>

- 540 [35] T. N. Miles, R. He, Temporal and spatial variability of Chl-a and SST
 541 on the South Atlantic Bight: Revisiting with cloud-free reconstructions
 542 of MODIS satellite imagery, *Continental Shelf Research* 30 (2010) 1951–
 543 1962. doi:10.1016/j.csr.2010.08.016.
- 544 URL <http://dx.doi.org/10.1016/j.csr.2010.08.016>
- 545 [36] D. Sirjacobs, A. Alvera-Azcárate, A. Barth, G. Lacroix, Y. Park,
 546 B. Nechad, K. Ruddick, J.-M. Beckers, Cloud filling of ocean colour
 547 and sea surface temperature remote sensing products over the South-
 548 ern North Sea by the Data Interpolating Empirical Orthogonal
 549 Functions methodology, *Journal of Sea Research* 65 (2011) 114–130.
 550 doi:10.1016/j.seares.2010.08.002.
- 551 URL <http://linkinghub.elsevier.com/retrieve/pii/S1385110110001036>
- 552 [37] J. N. Waite, F. J. Mueter, Spatial and temporal variability of
 553 chlorophyll-a concentrations in the coastal Gulf of Alaska, 1998–
 554 2011, using cloud-free reconstructions of SeaWiFS and MODIS-
 555 Aqua data, *Progress in Oceanography* 116 (2013) 179–192.
 556 doi:10.1016/j.pocean.2013.07.006.
- 557 URL <http://dx.doi.org/10.1016/j.pocean.2013.07.006>
- 558 [38] J.-M. Beckers, A. Barth, A. Alvera-Azcárate, DINEOF reconstruction
 559 of clouded images including error maps-application to the Sea-Surface
 560 Temperature around Corsican Island, *Ocean Science* 2 (2006) 183–199.

- 561 doi:10.5194/osd-3-735-2006.
- 562 URL <http://www.ocean-sci-discuss.net/3/735/2006/>
- 563 [39] D. L. Zimmerman, M. Stein, Classical Geostatistical Methods,
564 in: A. Gelfand, P. Diggle, M. Fuentes, P. Guttorp (Eds.),
565 Handbook of Spatial Statistics, Vol. 20103158 of Chapman &
566 Hall/CRC Handbooks of Modern Statistical Methods, 2010, pp. 29–44.
567 doi:10.1201/9781420072884.
- 568 [40] D. L. Zimmerman, M. B. Zimmerman, A Comparison of Spatial Semi-
569 variogram Estimators and Corresponding Ordinary Kriging Predictors,
570 Technometrics 33 (1) (1991) 77–91.
- 571 [41] R. H. Shumway, S. S. David, Time Series Analysis and Its Applications,
572 2011.
- 573 [42] P. Brasseur, Ocean data assimilation using sequential methods based
574 on the Kalman filter, in: Ocean Weather Forecasting, Springer Edition,
575 2006, pp. 271–316.

576 **List of Tables**

577 1	Spatial building blocks proposed by [1]	36
578 2	Temporal building blocks proposed by [1]	37
579 3	Parameters of the covariance model given in equation (28) 580 estimated by WLS.	38

Table 1: Spatial building blocks proposed by [1]

Function	Parameters
$\varphi_1(t) = \exp(-ct^\gamma)$	$c > 0, 0 < \gamma \leq 1$
$\varphi_2(t) = (2^{\nu-1}\Gamma(\nu))^{-1}(ct^{1/2})^\nu K_\nu(ct^{1/2})$	$c > 0, \nu > 0$
$\varphi_3(t) = (1 + ct^\gamma)^{-\nu}$	$c > 0, 0 < \gamma \leq 1, \nu > 0$
$\varphi_4(t) = 2^\nu(\exp(ct^{1/2}) + \exp(-ct^{1/2}))^{-\nu}$	$c > 0, \nu > 0$

Table 2: Temporal building blocks proposed by [1]

Function	Parameters
$\psi_1(t) = (at^\alpha + 1)^\beta$	$a > 0, 0 < \alpha \leq 1, 0 \leq \beta \leq 1$
$\psi_2(t) = \ln(at^\alpha + b)/\ln(b)$	$a > 0, b > 1, 0 < \alpha \leq 1$
$\psi_3(t) = (at^\alpha + b)/(b(at^\alpha + 1))$	$a > 0, 0 < b \leq 1, 0 < \alpha \leq 1$

Table 3: Parameters of the covariance model given in equation (28) estimated by WLS.

σ^2	τ	c	γ	a	α	β
0.08	0.82	0.45	0.10	0.1	1.0	0.92

581 **List of Figures**

582 1	Raw data plots: (a) map of average log-concentrations of CHL 583 between 1998 and 2004, (b) map of average percentage of miss- 584 ing data for each location between 1998 and 2006, and (c) 585 time-series of the percentage of missing data over the Red Sea 586 between 1998 and 2004.	41
587 2	Log-CHL concentration time-series for every pixel of the do- 588 main (blue curves). The red curve plots the spatially averaged 589 log-concentrations and the black curve plots the spatial aver- 590 age of the seasonal component. Both are computed from the 591 data filled with DINEOF.	42
592 3	Anomalies estimated by DINEOF for the first 8 weeks of 1998.	43
593 4	Anomaly times series (panels b to d) at three locations as 594 indicated in panel (a)	44
595 5	Description of the experimental setup.	45
596 6	RMS error over the cross-validation period for a varying num- 597 ber of smoothing iterations and number of EOFs. Crosses 598 indicate the minimal error for a given number of iterations.	46
599 7	EOF modes after the DINEOF data filling: (a) first spatial 600 EOF mode, (b) second spatial EOF mode, (c) first temporal 601 EOF mode, (d) second temporal EOF mode, (e) spatial av- 602 erage of the seasonal anomalies computed from the DINEOF 603 filled data, (f) cumulative sum of the percentage of variance 604 explained for the modes computed with DINEOF.	47
605 8	Fitting the covariance model to the space-time empirical covar- 606 iance matrix: (b) empirical space covariance function and 607 fitted space covariance functions, (c) empirical time covariance 608 function and fitted time covariance functions.	48
609 9	Contour plot of the empirical covariance function (dashed curves) 610 and of the fitted space-time covariance function (solid curves)	49
611 10	Results of the Kalman filter: (a) time series of RMS errors 612 of forecasts for the covariance model compared with a pure 613 seasonal prediction, (b) distribution of the prediction RMS 614 error over the three-year cross-validation period.	50

615	11	Predictions for the period between 24 October 2006 and 31		
616		October 2006 (a, b, c), and between 6 March 2006 and 14		
617		March 2006 (d, e, f): (a, d) plot the seasonal prediction, (b,		
618		e) the model prediction with the Kalman filter, and (c, f) the		
619		observations.	51	
620	12	Spatial averages over the validation period of: (a) the vari-		
621		ances of the prediction error resulting from by the reduced-		
622		order Kalman filter, and (b) the RMS errors.	52	
623	13	Diagnostic statistics of the filter: (a) increment distribution in		
624		space averaged over the validation period, (b) cumulative av-		
625		eraged innovation over time, (c) distribution of the innovation		
626		values for the validation period.	53	
627	14	Average correlation maps over the validation period between		
628		the observations and (a) the seasonal forecast, (b) the CHL		
629		forecasts (including the seasonal component), and (c) the filter		
630		analyses (including the seasonal component).	54	

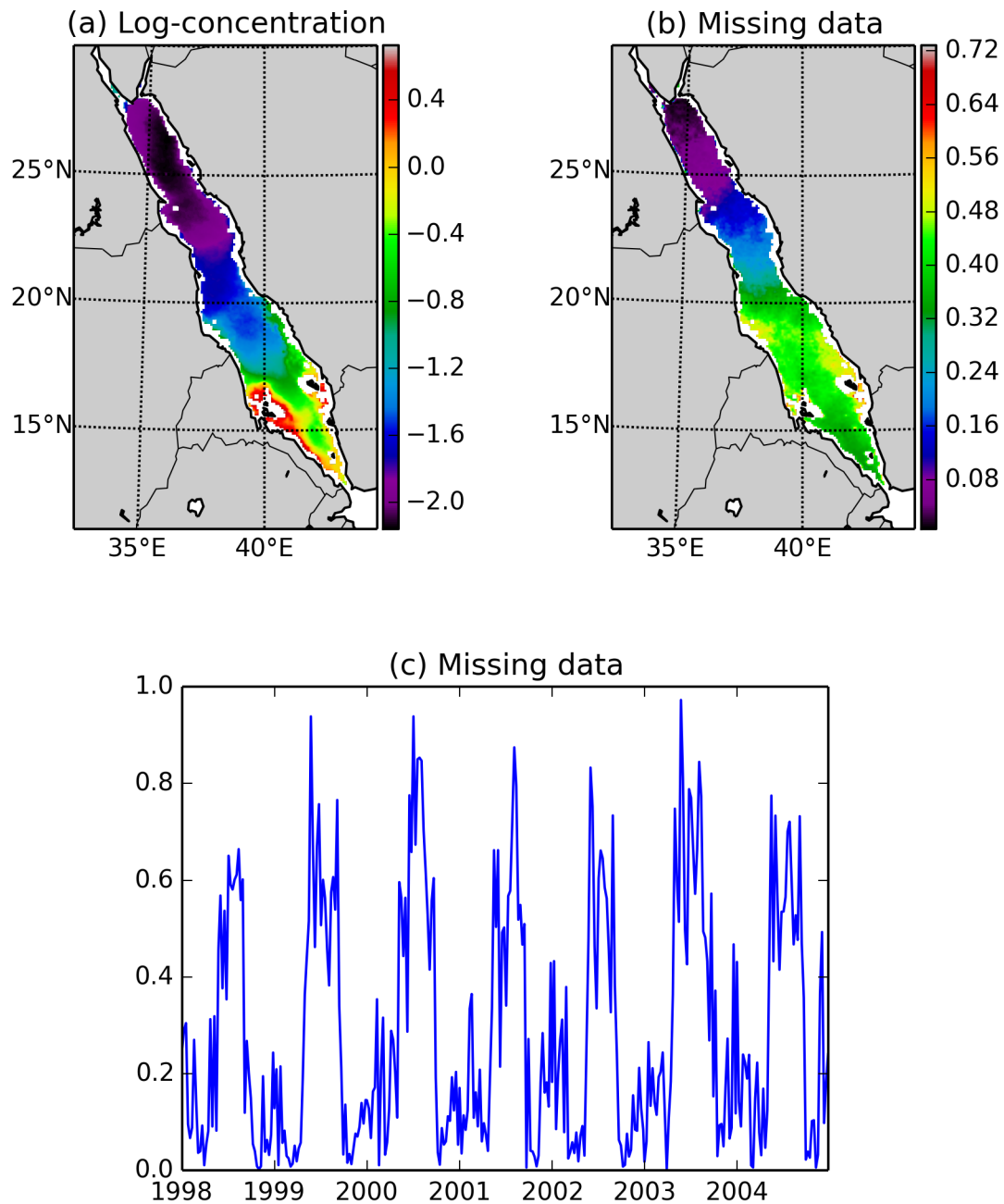


Figure 1: Raw data plots: (a) map of average log-concentrations of CHL between 1998 and 2004, (b) map of average percentage of missing data for each location between 1998 and 2006, and (c) time-series of the percentage of missing data over the Red Sea between 1998 and 2004.

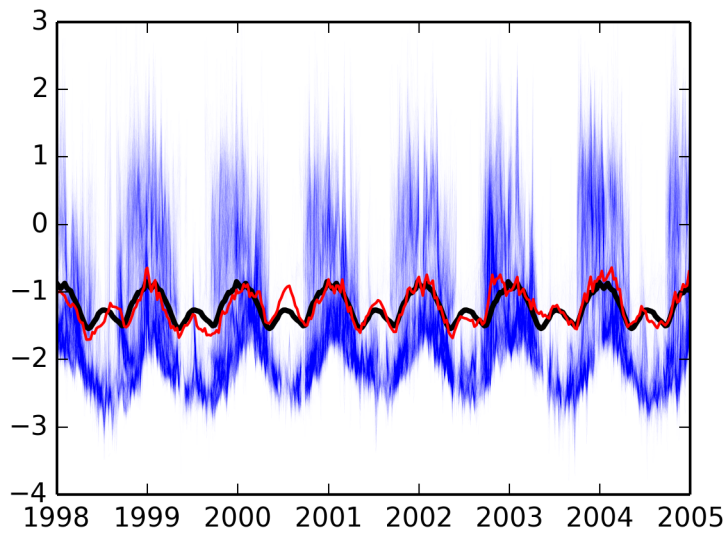


Figure 2: Log-CHL concentration time-series for every pixel of the domain (blue curves). The red curve plots the spatially averaged log-concentrations and the black curve plots the spatial average of the seasonal component. Both are computed from the data filled with DINEOF.

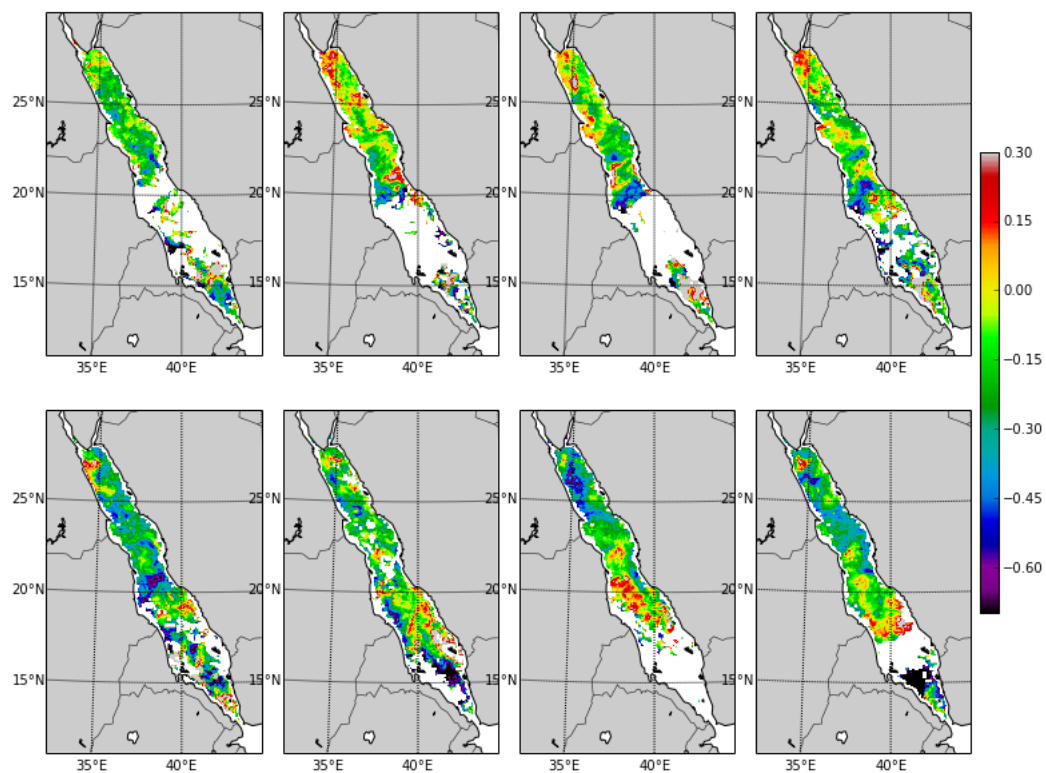


Figure 3: Anomalies estimated by DINEOF for the first 8 weeks of 1998.

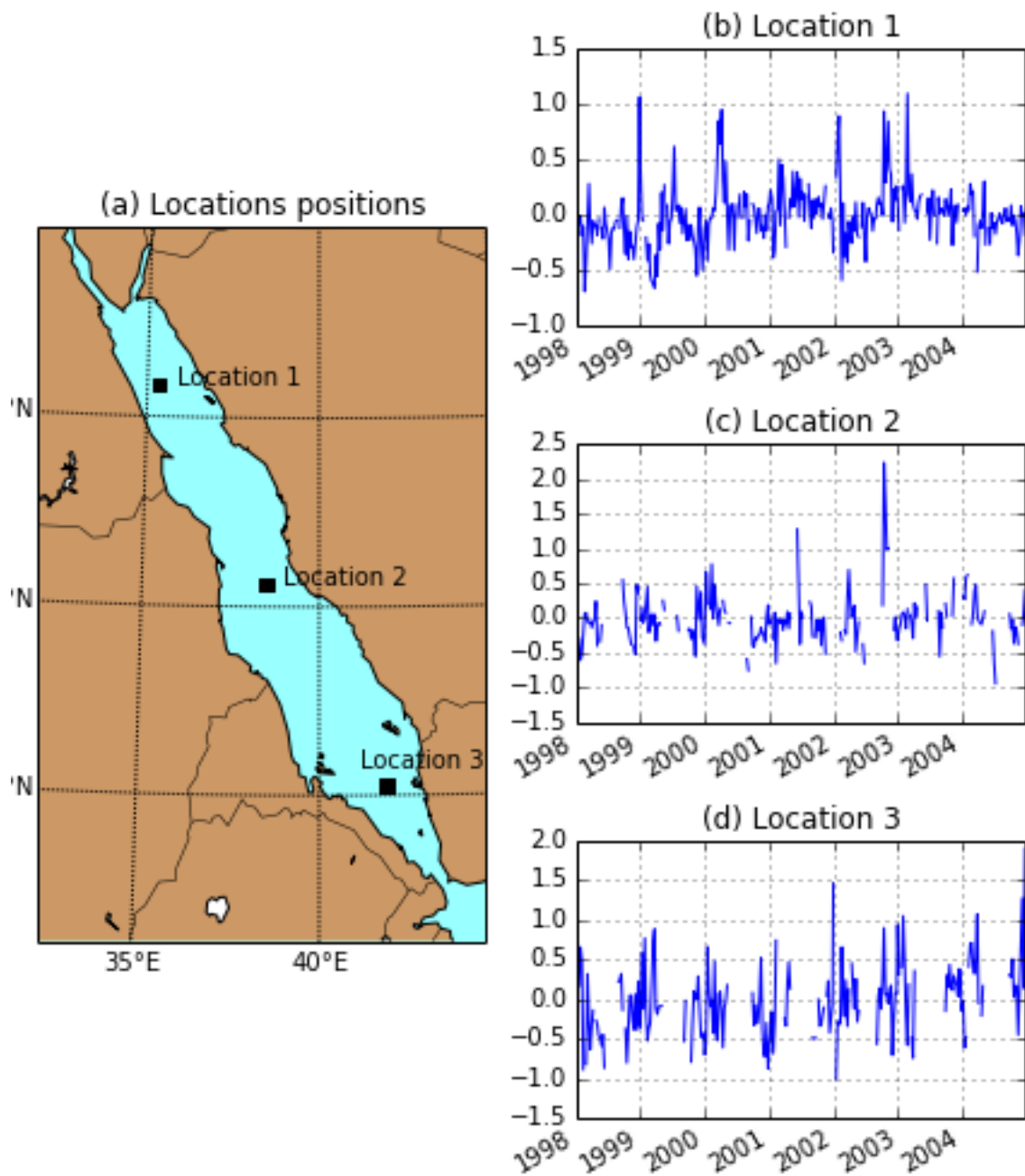


Figure 4: Anomaly times series (panels b to d) at three locations as indicated in panel (a)

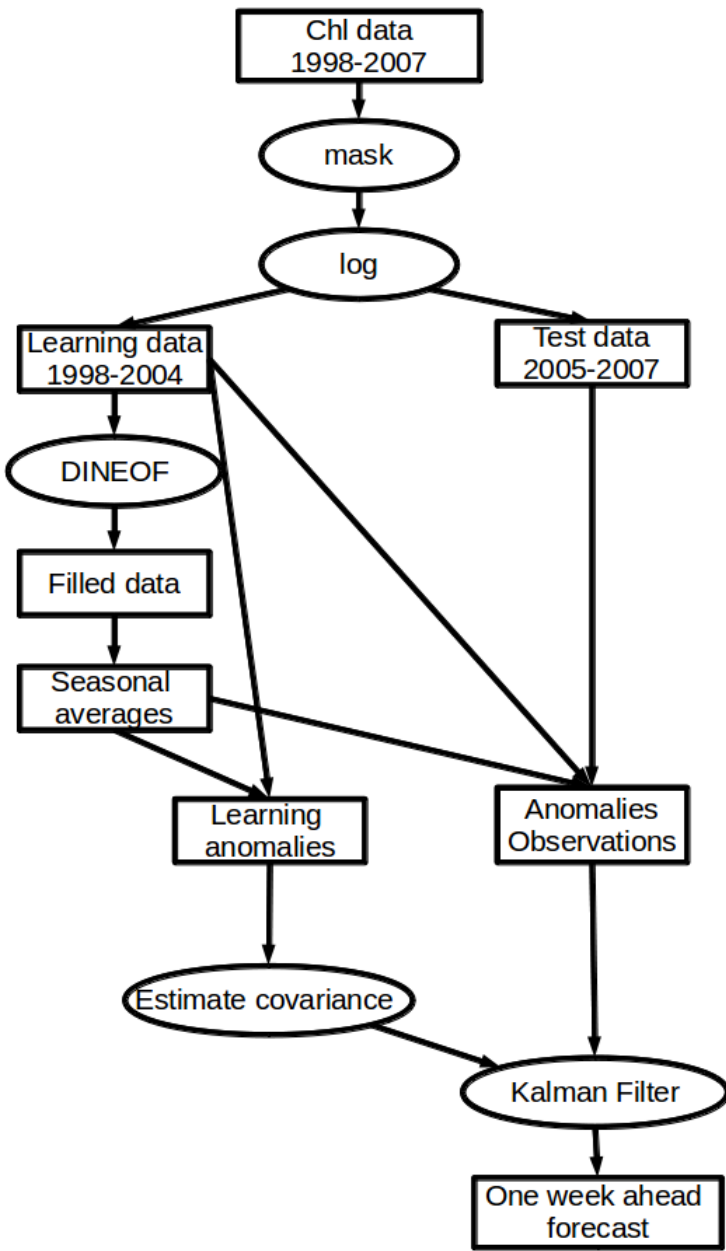


Figure 5: Description of the experimental setup.

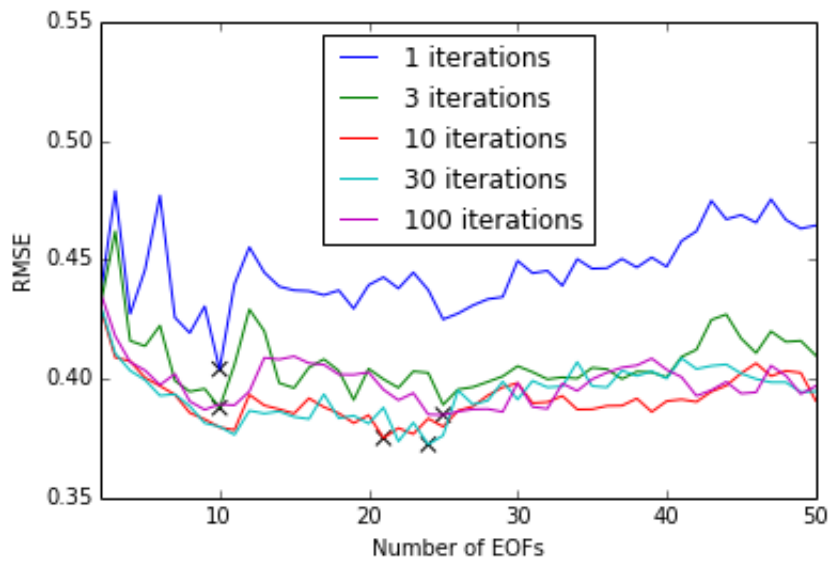


Figure 6: RMS error over the cross-validation period for a varying number of smoothing iterations and number of EOFs. Crosses indicate the minimal error for a given number of iterations.

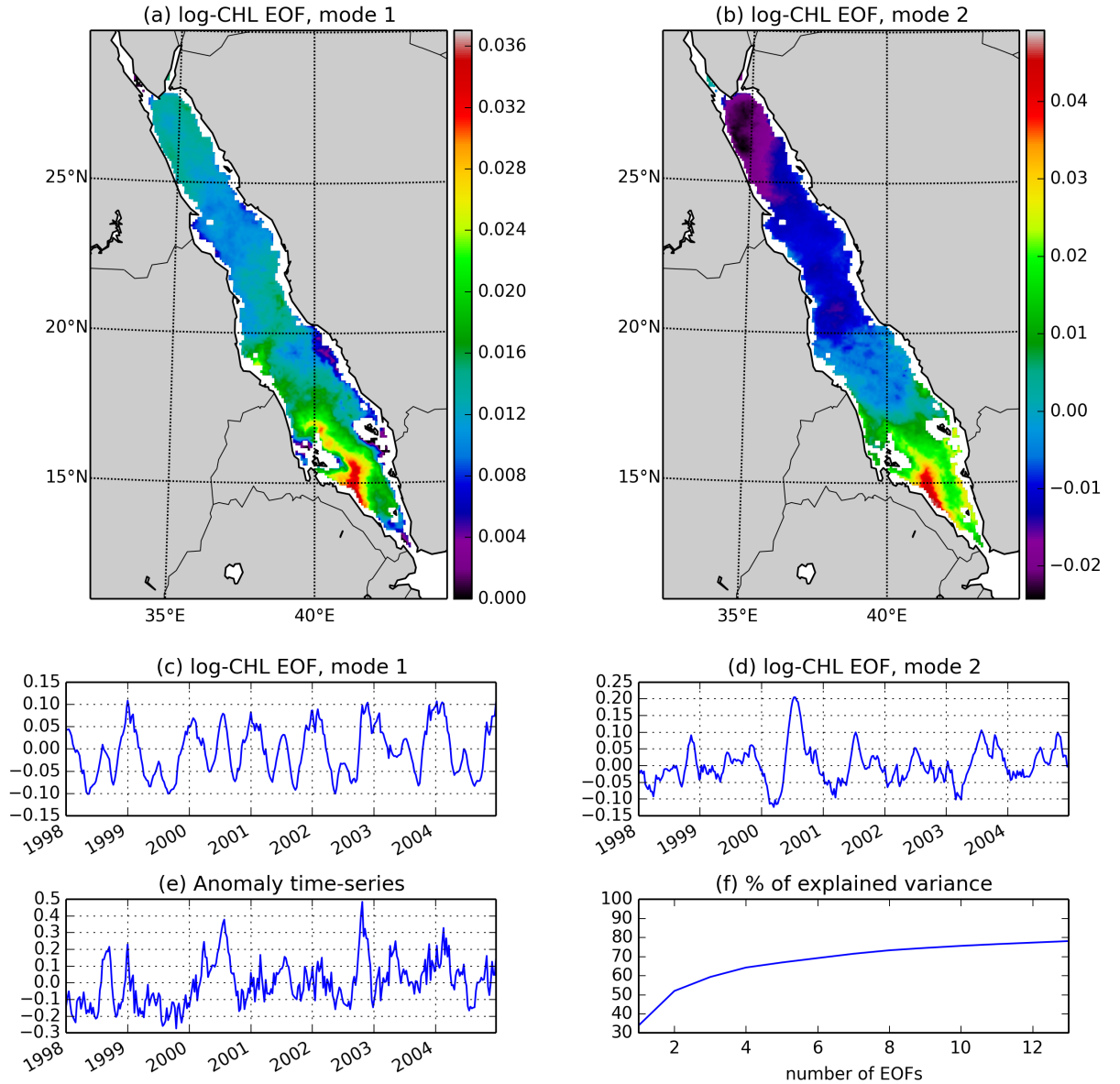


Figure 7: EOF modes after the DINEOF data filling: (a) first spatial EOF mode, (b) second spatial EOF mode, (c) first temporal EOF mode, (d) second temporal EOF mode, (e) spatial average of the seasonal anomalies computed from the DINEOF filled data, (f) cumulative sum of the percentage of variance explained for the modes computed with DINEOF.

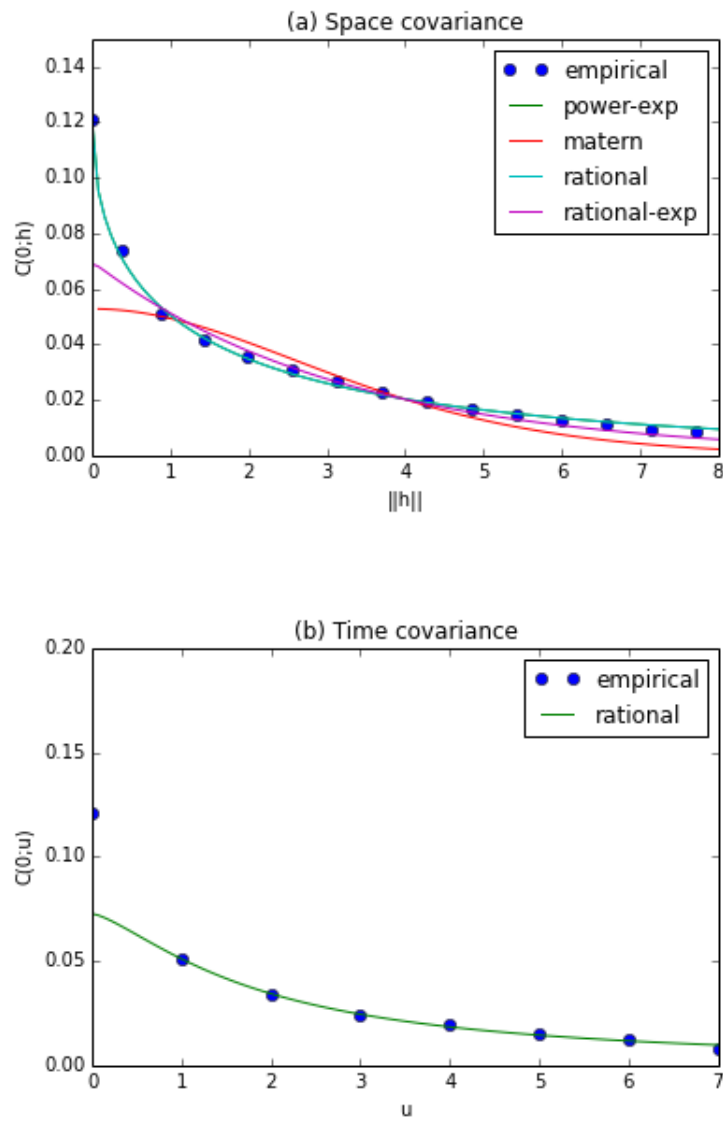


Figure 8: Fitting the covariance model to the space-time empirical covariance matrix: (b) empirical space covariance function and fitted space covariance functions, (c) empirical time covariance function and fitted time covariance functions.

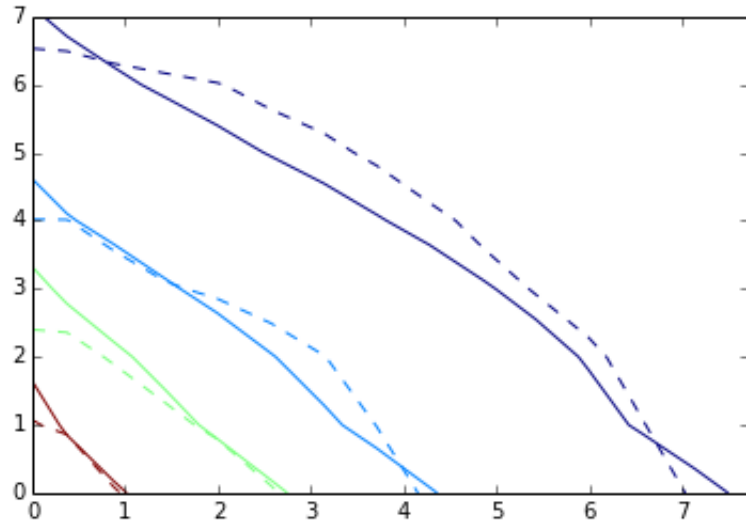


Figure 9: Contour plot of the empirical covariance function (dashed curves) and of the fitted space-time covariance function (solid curves)

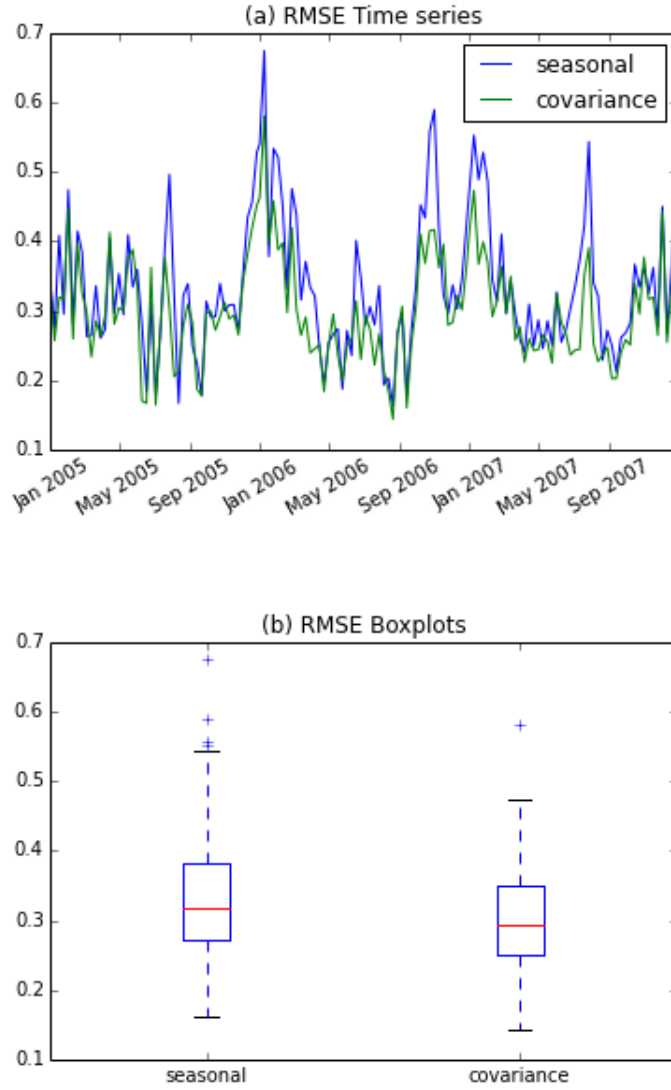


Figure 10: Results of the Kalman filter: (a) time series of RMS errors of forecasts for the covariance model compared with a pure seasonal prediction, (b) distribution of the prediction RMS error over the three-year cross-validation period.

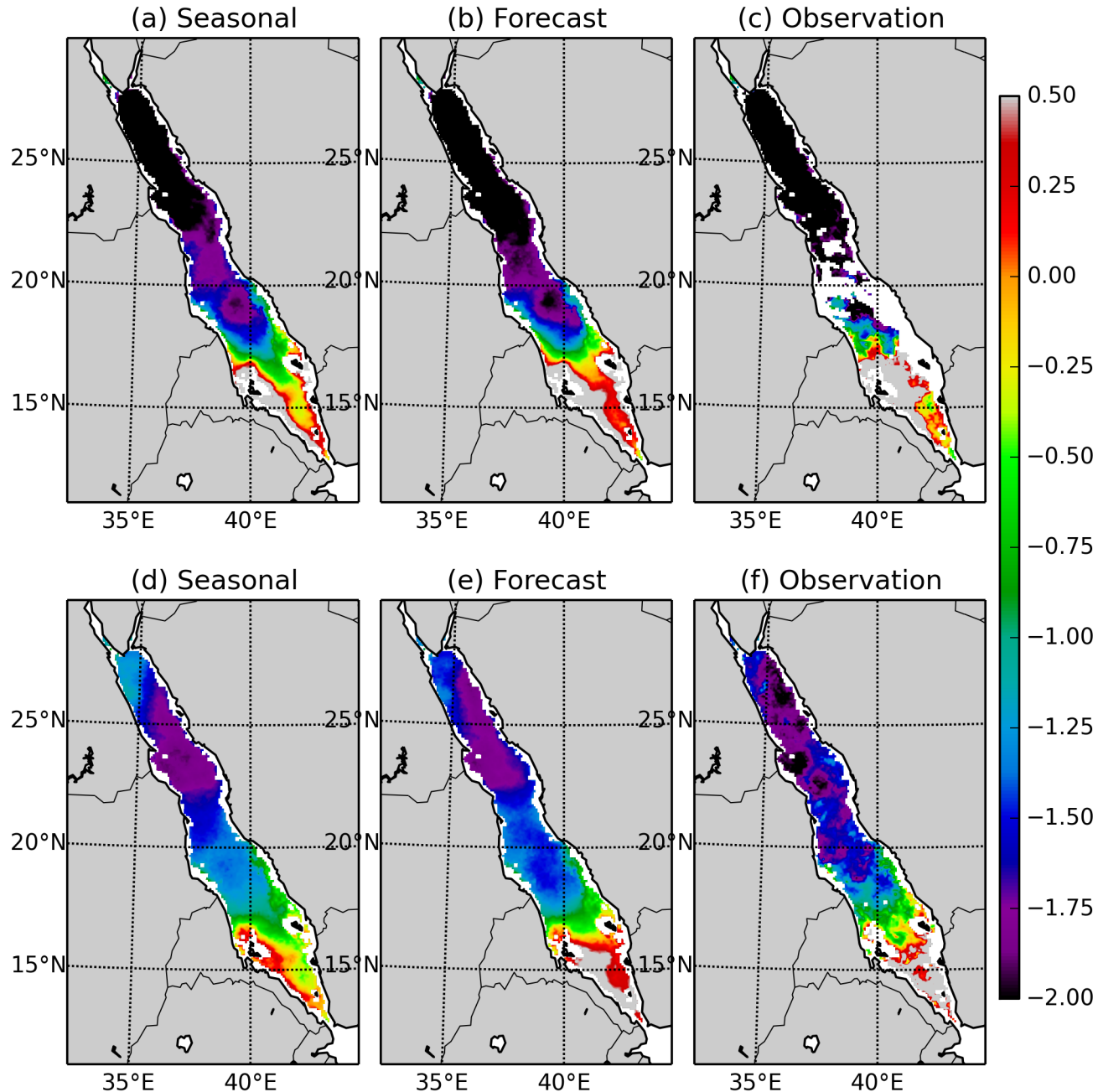


Figure 11: Predictions for the period between 24 October 2006 and 31 October 2006 (a, b, c), and between 6 March 2006 and 14 March 2006 (d, e, f): (a, d) plot the seasonal prediction, (b, e) the model prediction with the Kalman filter, and (c, f) the observations.

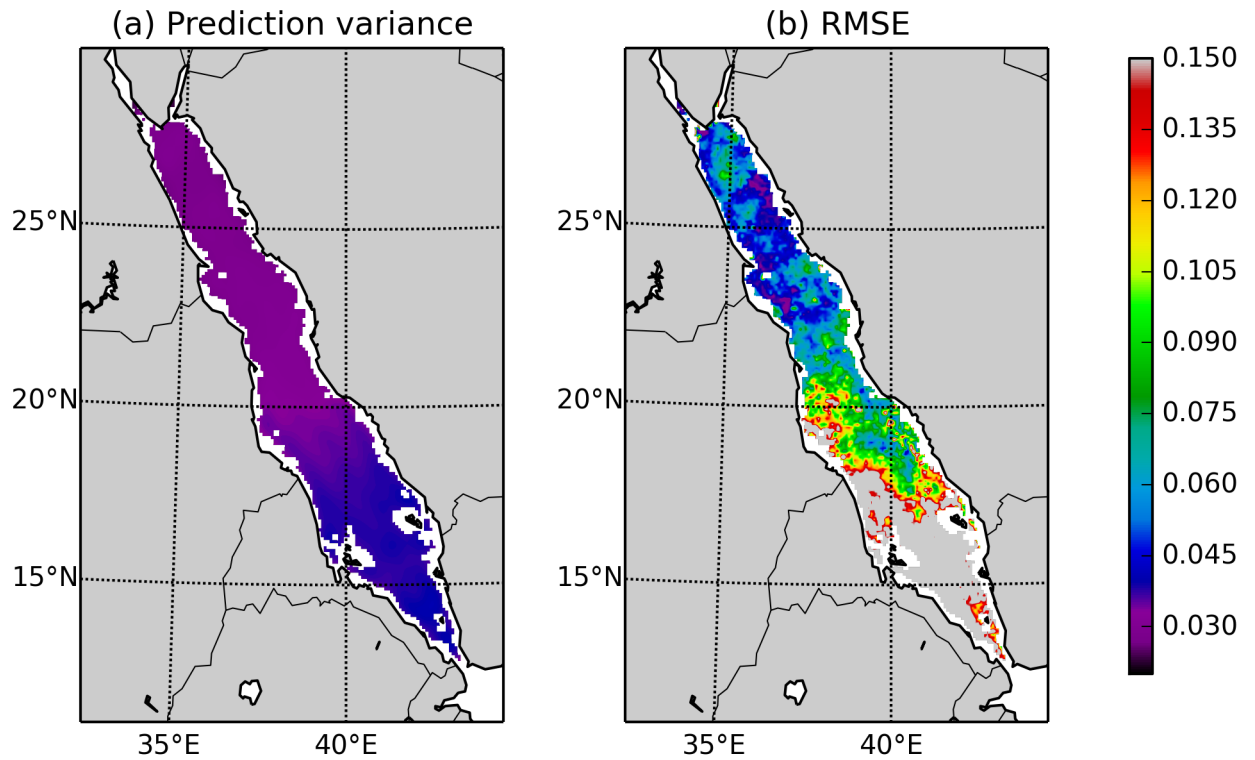


Figure 12: Spatial averages over the validation period of: (a) the variances of the prediction error resulting from by the reduced-order Kalman filter, and (b) the RMS errors.

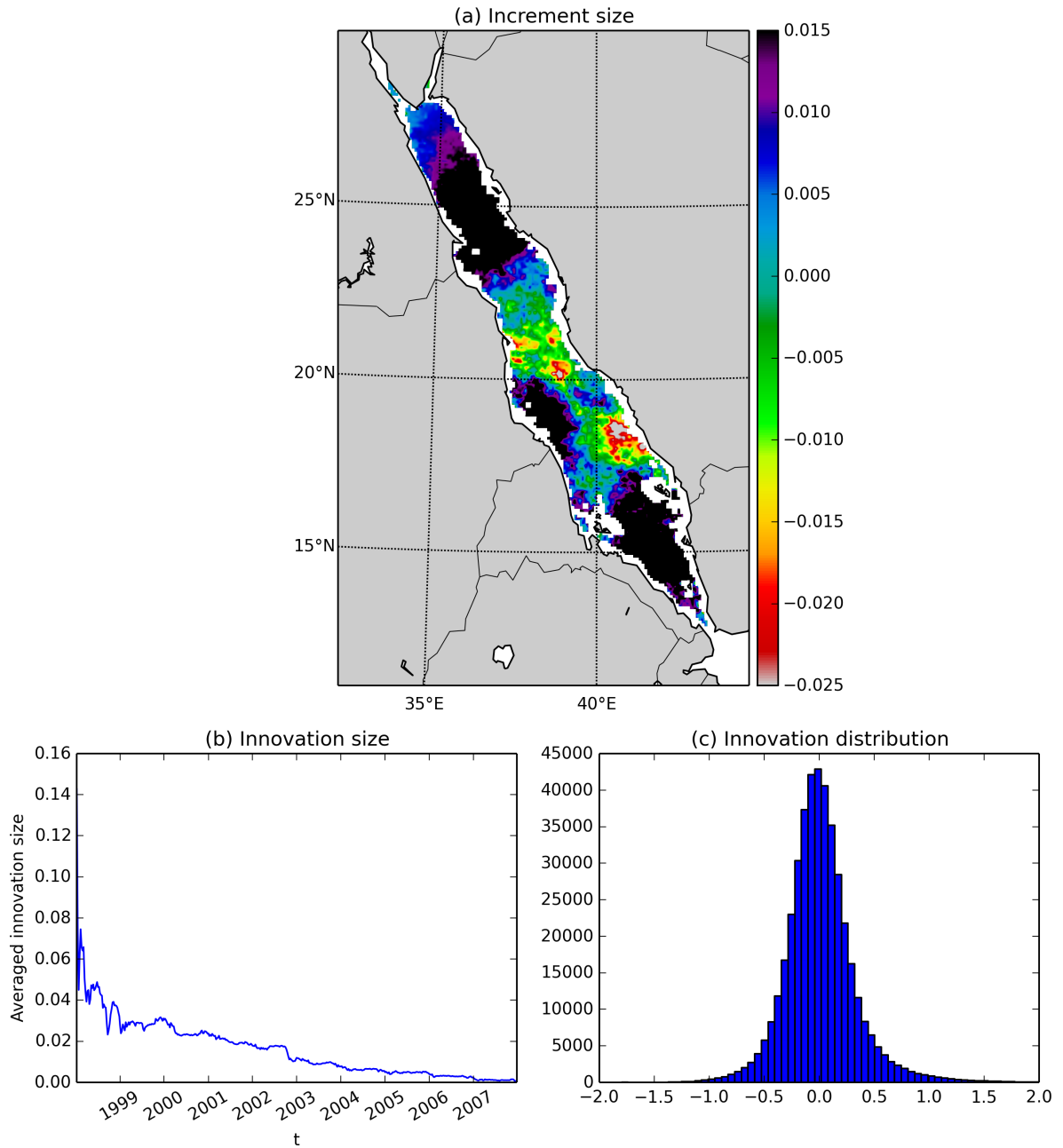


Figure 13: Diagnostic statistics of the filter: (a) increment distribution in space averaged over the validation period, (b) cumulative averaged innovation over time, (c) distribution of the innovation values for the validation period.

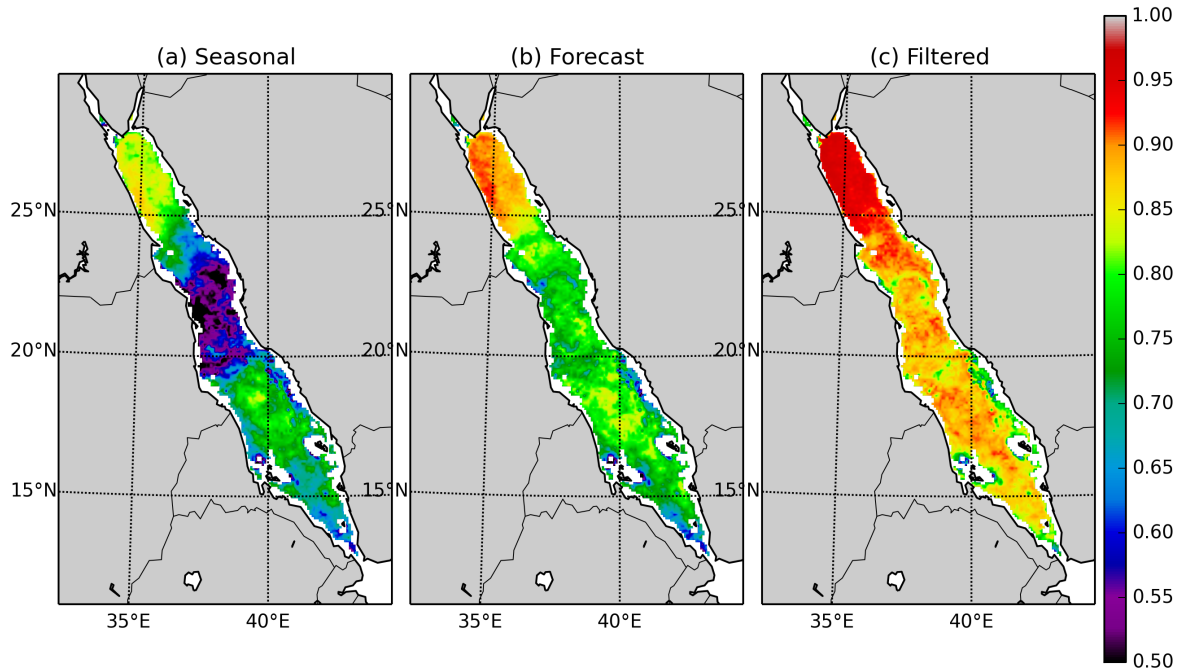


Figure 14: Average correlation maps over the validation period between the observations and (a) the seasonal forecast, (b) the CHL forecasts (including the seasonal component), and (c) the filter analyses (including the seasonal component).